Variational Arbitrary Lagrangian-Eulerian method

Thesis by

Pururav Thoutireddy

In Partial Fulfillment of the Requirements

for the Degree of

Doctor of Philosophy

California Institute of Technology

Pasadena, California

2003

(Defended October 07, 2002)

To my aunt

Sulochana Kunduru

and

my parents

Madhusudhan Reddy Thoutireddy and Vijayalaxmi Thoutireddy.

Acknowledgements

I would like to take this opportunity to express my deep gratitude to my advisor, Prof. Michael Ortiz, for his patience, guidance, and support. His inexhaustible wealth of ideas is but one of the many reasons for my admiration.

I am also thankful for the support of the Office of Naval Research, Department of Energy and Army Research Office.

I am indebted to Profs. Ravichandran, Bhattacharya, Rosakis and Marsden for sharing with me their wealth of knowledge and for their encouragement.

I would like to thank my friends Eduardo, Matt, Fehmi, Bill, Marisol, Adrian, Raul, Enzo to whom I owe my enjoyment at work. I also would like to thank Aamod, MA, Dnyanesh, Mandar and Tamim who made my stay at CALTECH very pleasant.

Abstract

This thesis is concerned with the development of Variational Arbitrary Lagrangian-Eulerian method (VALE) method. VALE is essentially finite element method generalized to account for horizontal variations, in particular, variations in nodal coordinates. The distinguishing characteristic of the method is that the variational principle simultaneously supplies the solution, the optimal mesh and, in case problems of shape optimization, optimal shape. This is accomplished by rendering the functional associated with the variational principle stationary with respect to nodal field values as well as with respect to the nodal positions of triangulation of the domain of analysis. Stationarity with respect to the nodal positions has the effect of the equilibriating the energetic or configurational forces acting in the nodes. Further, configurational force equilibrium provides precise criterion for mesh optimality. The solution so obtained corresponds to minimum of energy functional (minimum principle) in static case and to the stationarity of action sum (discrete Hamilton's stationarity principle) in dynamic case, with respect to both nodal variables and nodal positions. Further, the resulting mesh adaption scheme is devoid of error estimates and mesh-to-mesh transfer interpolation errors. We illustrate the versatility and convergence characteristics of the method by way of selected numerical tests and applications, including the problem of semi-infinite crack, the shape optimization of elastic inclusions and free vibration of 1-d rod.

Contents

List of Figures

List of Tables

Chapter 1

Introduction

Numerical solution for the discretized continuum is dependent on mesh. For the case of inhmogeneous system the numerical solution is also dependent material configuration. Considreration of configurational forces provides elegant framework for the investigation of such a dependency and enables solution of optimal mesh and material configuration where applicable.

1. **Mesh Adaption**: The response of continuum often exhibits multiple length scales. This may be due to a variety of causes, including i) strong discontinuities in the solution made possible by the hyperbolicity of the problem, e.g., localization shocks, slip lines; ii) steep gradients due to mathematical singularities as in the case of solution near the crack-tip in fracture mechanics; iii) the simultaneous operation of interacting mechanisms possessing vastly disparate length scales, as in the case when the small or microscopic-length scale determines the behavior of the system at the large or macroscopic-length scales. Further applications involving fully unconstrained flows of material are amenable to a fully Lagrangian finite element solution, provided that the inevitable deformation-induced distortion is eliminated by recourse to continuous mesh adaption. To account for these effects, a number of strategies for remeshing have been developed, most of which include error estimation and mesh-to-mesh transfer [20, 21, 22, 26]. In the work of Radovitzky and Ortiz [20] local posteriori error estimates are computed, which inturn provide mesh-size distribution. Based on this mesh-size distribution, whole computational domain is remeshed and fields are transferred from the previous mesh to the new mesh. Molinari and Ortiz [21] used the local error estimates so obtained to decide which elements need refinement or coars-

ening based on assumed thresholds on the error indicators. Then mesh refinement and coarsening are accomplished semilocally based on Longest edge propagation path (LEPP) [47], with localized mesh-to-mesh transfer. Due to the localized nature of mesh-to-mesh transfer, interpolation errors are limited to the elements which have been effected by the mesh refinement/coarsening. In the work of Shephard [26] mesh adaption is accomplished with strain energy density variation as error indicator and mesh adaption is accomplished either by remeshing or relocating nodes interactively. All the above methods need mesh-to-mesh transfer, which involves interpolation error during the transfer of fields from old mesh to new mesh. Further, fields on the new mesh are not guaranteed to satisfy the nodal force equilibrium. The error associated with mesh-to-mesh transfer, coupled with nodal force non-equilibrium, may cause numerical instability of the simulation. In fact this is the motivation for the development of this method. In our previous research for the development of velocity-variational Lagrangian formulation for fluids [34], accumulation of mesh-to-mesh transfer errors caused instability of the simulation. This necessitated development of a mesh adaption scheme which does not involve mesh-to-mesh transfer.

One of the popular methods based on nodal relocation is gradient-weighted moving finite element (GWMFE) developed by Miller et al. [30, 31]. This is an improved version of moving finite element method (MFE) [32]. In GWMFE, evolution of nodal coordinates is assumed to satify PDE for normal motion. Even though this scheme does not involve error estimation and mesh-to-mesh transfer, it is not variational.

2. **Shape/Structural optimization**: In case of inhomogeneous system continuum response is sensitive to material configuration. One such important application is the shape optimization for obtaining equilibrium shape, i.e., inclusion shape corresponding to minimum energy functional of the inhomogeneous material system. Most of the methods [23, 24] developed for accomplishing shape optimization are not general enough to account for all possible loading conditions and are developed for linearized kinematics. The method developed by Jog et al. [18] has no limitation with regard to loading conditions but still has limitation of linearized kinematics. However, finite deformation effects could be important, as in the case of interaction of material interface with free surface.

To address these issues we propose Variational Arbitrary Lagrangian-Eulerian (VALE) method. VALE method is essentially finite element method generalized to account for horizontal variations (variations in undeformed or nodal coordinates). The distinguishing characteristic of the method is that the variational principle simultaneously supplies the solution, the optimal mesh and, in problens of shape optimization, the optimal shape of the system. This is accomplished by rendering vatiational functional stationary with respect to nodal field values as well as with respect to the nodal coordinates of the triangulation of the domain of analysis. These stationarity conditions correspond to nodal force balance and nodal configurational/material [14, 1, 2] force balance, respectively (in this thesis, we use configurational force and material force interchangeably and both mean the same). Similarly in dynamics, stationarity of action sum with respect to time component of horizontal variations provides time adaption and this condition correspond to energy conservation [13] for conservative systems. However, the resulting equation, which can be solved for the corresponding time step, is very non-linear and numerically expensive. Further, the resulting variational integrator, even without solving for time step, has good long-term energy behavior. So, in this thesis we will not consider time component of horizontal variations.

The ability of VALE method to account for horizontal variations enables the solution for the nodal coordinates. The resulting mesh adaption scheme is devoid of error estimates and mesh-to-mesh transfer, and hence the concomitant interpolation errors. Further, the configurational nodal force equilibrium provides the precise criterion for mesh optimality. The mesh so obtained is the optimal mesh in the sense that the solution for deformed coordinates so obtained is the most accurate solution for a given number of nodes. Also, the deformed coordinate solution after mesh adaption is guaranteed to satisfy nodal force equilibrium and hence preserves mechanical structure.

In the second chapter of this thesis, we demonstrate the VALE method as a mesh adaption scheme. For homogeneous material in the continuous case, energy functional possesses translational symmetry in reference configuration. However, in the discrete case, translational symmetry of energy functional with respect to nodal coordinates is broken as a consequence of introduction of discretization. The resulting stationarity condition provides a system of equations which enable solution of nodal coordinates. We demonstrate the ability of the resulting mesh adaption scheme to resolve steep gradients in the presence of singularity by applying it to fracture mechanics problems and neohookean elastic solid

subjected to moving point load. Also, since the analytic/exact solution for the linear-elastic case is known, we study the convergence behavior with mesh adaption and compare it without mesh adaption. Here, it is observed, that mesh adaption not only reduces error but also provides faster convergence. Since J-integral can be interpreted to be the material force corresponding to the crack-tip node in the tangential direction of the crack face, J-integral evaluation can be accomplished in a natural manner without any contour or domain integral evaluation. J-integral so evaluated is very accurate.

In the third chapter of the thesis, we demonstrate VALE's application to shape optimization, specifically equilibrium shape of a misfitting particle in a matrix. In this case in addition to discretization, inhomogeneity also contributes to the breaking of translational symmetry of energy functional with respect to nodal coordinates. In particular the corresponding continuous case also, energy functional does not possess translational symmetry with respect to undeformed coordinates. The shape optimization capability of the algorithm has been demonstrated with the study of the symmetry-breaking transition phenomena associated with dilatational misfit.

In the fourth chapter, we demonstrate this method's application as a variational integrator with horizontal variations. To obtain the update for nodal coordinates we render space-time discretized action sum stationary with respect to nodal coordinates, in addition to deformed coordinates. The additional system of equations provides the update for nodal coordinates. The resulting algorithm is symplectic-momentum preserving [28] and has good long-term energy behavior. Since nodal coordinates themselves are the solution, this method can be applied to simulations involving moving gradients. In particular we demonstrate its application to shock capturing, wherein the ability of nodes to focus on moving shock has been demonstrated. Further, good long-term energy behavior has been observed.

One of the advantages of the variational integrators with horizontal variations in the context of contact-impact simulation is the bigger stable time-step for the efficient numerical simulation. It will also help if the element used for the finite element computation has well-defined lumped masses and contact tractions. To accomplish this, in the fifth chapter, we develop and analyze a composite 'CT3D' tetrahedral element. This element consists of an ensemble of twelve 4-node linear tetrahedral elements, coupled to a linear assumed deformation defined over the entire domain of the composite element. The element is

designed to have well-defined lumped masses and contact tractions in dynamic contact problems while at the same time minimizing the number of volume constraints per element. The relation between displacements and deformations is enforced weakly by recourse to the Hu-Washizu principle. The element arrays are formulated in accordance to the 'assumed-strain' prescription. The formulation of the element accounts for fully nonlinear kinematics. Integrals over the domain of the element are computed by a five-point quadrature rule. The element passes the patch test in arbitrarily distorted configurations. Our numerical tests demonstrate that CT element has been found to possess convergence rate comparable to those of linear simplicial elements, and that these convergence rates are maintained as the near-incompressible limit is approached. We have also verified that the element satisfies the Babuška-Brezzi condition for a regular mesh configuration. These tests suggest that the CT3D element can indeed be used reliably in calculations involving near-incompressible behavior such arises, e.g., in the presence of unconfined plastic flow.

Chapter 2

Mesh adaption

2.1 Introduction

Mesh adaption becomes necessary for efficient numerical solution, especially in the presence of steep gradients as in the case of singularities in the case fracture problems, shock capture in wave propagation, etc.. Further applications involving fully unconstrained flows of material are amenable to a fully Lagrangian finite element solution provided that the inevitable deformation-induced distortion is eliminated by recourse to continuous mesh adaption. However the present schemes [20, 21] are not robust enough due to mesh-to-mesh transfer with concomitant interpolation errors and nodal force non-equilibrium. Further, these methods do not possess precise mesh optimality criterion and may not provide the optimal mesh. To remedy this we propose and develop a novel method, Variational Arbitrary Lagrangian-Eulerian (VALE) which is devoid of these deficiencies. The resulting mesh adaption scheme is variationally consistent and is devoid of error estimation and mesh-to-mesh transfer, hence interpolation errors. Further, mesh so obtained is the optimal mesh in the sense that it provides the most accurate solution for a given number of nodes.

In this chapter, we demonstrate one of its most important applications as a tool for mesh adaption with elastic material as prototype material.To this end we begin by developing variational formulation for an elastic solid.

2.2 Variational formulation

We consider a solid occupying a region $B_0 \in \mathbb{R}^3$ in its reference undeformed configuration. The solid subsequently deforms under the action of externally applied forces and prescribed

displacements. The deformation mapping $\boldsymbol{\varphi} : B_0 \to \mathbb{R}^3$ maps material points $\boldsymbol{X}$ in the reference configuration into their corresponding positions $\boldsymbol{x}$ in the deformed configuration $B = \boldsymbol{\varphi}(B_0)$. The deformation gradient field follows as $\boldsymbol{F} = \nabla_0 \boldsymbol{\varphi}$, where ∇_0 is the material gradient. In components:

$$F_{iJ} = \frac{\partial \varphi_i}{\partial X_J}, \quad \text{in } B_0 \tag{2.1}$$

Here and subsequently, we use upper (respectively, lower) case indices to denote components of vector fields defined over the undeformed (respectively, deformed) configuration. The deformation mapping is prescribed to take a prescribed value $\bar{\boldsymbol{\varphi}}$ over the displacement part ∂B_{01} of the undeformed boundary. This furnishes the boundary condition:

$$\varphi_i = \bar{\varphi}_i, \quad \text{on } \partial B_{01} \tag{2.2}$$

Additionally, the solid is in equilibrium, which requires

$$P_{iJ,J} + \rho_0 B_i = 0, \quad \text{in } B_0 \tag{2.3}$$

and

$$P_{iJ} N_J = \bar{T}_i, \quad \text{on } \partial B_{02} \tag{2.4}$$

Here $\boldsymbol{P}$ denotes the first Piola-Kirchhoff stress tensor, ρ_0 is the mass density per unit undeformed volume, $\boldsymbol{B}$ is the body force density per unit mass, $\boldsymbol{N}$ is the unit normal to the undeformed boundary, and $\bar{\boldsymbol{T}}$ is the applied traction over the traction boundary $\partial B_{02} = \partial B_0 - \partial B_{01}$. For simplicity, we shall assume that the material is elastic, with strain-energy density $W(\boldsymbol{F})$. Under these assumptions, the constitutive relations take the form:

$$P_{iJ} = \frac{\partial W}{\partial F_{iJ}}(\boldsymbol{F}) \equiv P_{iJ}(\boldsymbol{F}) \tag{2.5}$$

With a view to formulating finite-element approximations, we begin by re-stating the preceding equations in variational form.

$$I = \int_{B_0} W(\nabla_0 \boldsymbol{\varphi}) dV_0 - \int_{B_0} \rho_0 \boldsymbol{B} \cdot \boldsymbol{\varphi} dV_0 - \int_{\partial B_{02}} \bar{\boldsymbol{T}} \cdot \boldsymbol{\varphi} dS_0 \tag{2.6}$$

The functional is discretized by the introduction of a finite-element interpolation of the

form:

$$\boldsymbol{\varphi}_h(\boldsymbol{X}) = \sum_{a=1}^{N} \boldsymbol{x}_a N_a(\boldsymbol{X}) = \sum_{a=1}^{n} \boldsymbol{x}_a^e N_a^e(\boldsymbol{X}) \tag{2.7}$$

where $X \in \Omega^e$, Ω^e domain of the element e, N total number of nodes and n number of node per element. We further restrict attention to isoparametric element and consider element shape functions are of the form:

$$N_a^e = \hat{N}_a^e \circ \boldsymbol{\eta}^{e-1} \tag{2.8}$$

where

$$\boldsymbol{\eta}^e(\hat{\boldsymbol{X}}) = \sum_{a=1}^{n} \boldsymbol{X}_a \hat{N}_a(\hat{\boldsymbol{X}}) \tag{2.9}$$

is the isoparametric mapping for element e, defined over the standard domain $\hat{\Omega}$ of the element. Even though we used isoparametric element, which is usually the choice of elements, this formulation is independent of the choice of element and is equally valid for other types of elements such as composite element, details of which are given in Chapter 5. The discretized energy function:

$$I_h = \int_{B_0} W(\nabla_0 \boldsymbol{\varphi}_h) dV_0 - \int_{B_0} \rho_0 \boldsymbol{B} \cdot \boldsymbol{\varphi}_h dV_0 - \int_{\partial B_{02}} \bar{\boldsymbol{T}} \cdot \boldsymbol{\varphi}_h dS_0 \tag{2.10}$$

In finite element method we seek the minimum solution of I_h over a mesh [3]. Let this minimum be E_1 for a uniform mesh M_1, Fig. 2.1. Consider mesh M_2 which is obtained by relocating the nodes of mesh M_1 to the region of steep gradients (in this case close to crack tip) from regions of low gradients, while keeping everything else (number of nodes, number of elements and connectivity) same, which gives lower minimum E_2. Since analytic solution bounds numerical solutions from below, lower is the minimum energy I_h of the numerical solution, closer is the numerical solution to the analytic solution and hence less error. This suggests, to get the most accurate solution for a given number of nodes we need to seek minimum solution of I_h in the combined space of deformed $\boldsymbol{x}_h \equiv \{\boldsymbol{x}_a, a = 1, \ldots, N\}$ and undeformed $\boldsymbol{X}_h \equiv \{\boldsymbol{X}_a, a = 1, \ldots, N\}$ coordinates. Henceforth, the aim is to minimize I_h with respect to $\{\boldsymbol{x}_h, \boldsymbol{X}_h\}$ to get the most accurate solution possible. The stationarity condition corresponding to the minimum is

$$\langle DI_h, \delta \boldsymbol{x}_h \rangle \cdot \delta \boldsymbol{x}_h + \langle DI_h, \delta \boldsymbol{X}_h \rangle \cdot \delta \boldsymbol{X}_h = 0 \tag{2.11}$$

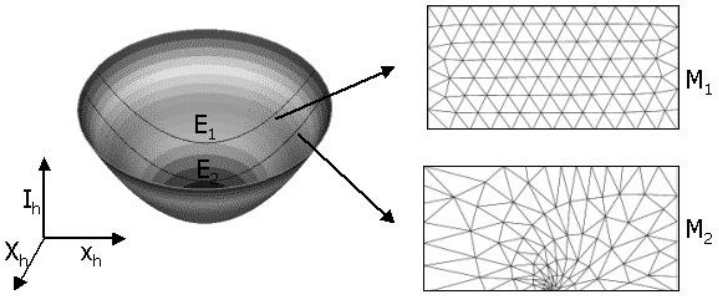

Figure 2.1: Dependence of minima on nodal coordinates

and since $\delta \boldsymbol{x}_h$ and $\delta \boldsymbol{X}_h$ are independent everywhere except on Dirichlet boundary,

$$\boldsymbol{r} = \langle DI_h, \delta \boldsymbol{x}_h \rangle = \frac{\partial I_h}{\partial \boldsymbol{x}_h} = 0 \quad : \quad \text{Nodal force equilibrium} \tag{2.12}$$

$$\boldsymbol{R} = \langle DI_h, \delta \boldsymbol{X}_h \rangle = \frac{\partial I_h}{\partial \boldsymbol{X}_h} = 0 \quad : \quad \text{Configurational nodal force equilibrium} \tag{2.13}$$

which enforce equilibria of nodal forces and nodal configurational (material) forces [2, 1], respectively.

Here nodal configurational force equilibrium (2.13) is as fundamental as nodal force equilibrium (2.12) and also furnishes the precise criterion for the mesh optimality. Further, the system of nodal configurational force equilibrium equations, in which number of equations is same as the number of undeformed coordinates degrees of freedom, together with nodal force equilibrium system of equations, provide a coupled system of equations for the simultaneous solution of the deformed ($\boldsymbol{x}_h$) and undeformed ($\boldsymbol{X}_h$) coordinates. It may be noted that in case of dynamics, similar stationarity conditions of discrete action sum corresponding to Hamilton's stationarity principle provide variational update for deformed and undeformed (nodal) coordinates at each time step and is discussed in Chapter 4.

On the Dirichlet boundary $\delta \boldsymbol{x}_h$ and $\delta \boldsymbol{X}_h$ are not independent, and the relation is given

by

$$\delta x_{ia} = \frac{\partial \bar{x}_i}{\partial X_I} \delta X_{Ia} \tag{2.14}$$

where $\bar{\boldsymbol{x}}(\boldsymbol{X})$ is the prescribed deformation on Dirichlet boundary and the corresponding nodal configurational equilibrium equations for Dirichlet boundary nodes are

$$\frac{\partial I_h}{\partial X_{Kb}} + \frac{\partial \bar{x}_k}{\partial X_K} \frac{\partial I_h}{\partial x_{kb}} = 0 \tag{2.15}$$

As can be expected nodes on Dirichlet boundary do not satisfy nodal force equilibrium, 'reaction force'. Since $r_{kb} = \frac{\partial I_h}{\partial x_{kb}}$ previous equation can also be expressed as

$$\frac{\partial I_h}{\partial X_{Kb}} + \frac{\partial \bar{x}_k}{\partial X_K} r_{kb} = 0 \tag{2.16}$$

In order to further explicate the stationarity conditions we begin by expressing the discretized energy in the form:

$$\begin{aligned} I_h = \sum_{e=1}^{E} \left\{ \int_{\Omega_0^e} W(\nabla_0 \boldsymbol{\varphi}_h) dV_0 - \int_{\Omega_0^e} \rho_0 \boldsymbol{B} \cdot \boldsymbol{\varphi}_h dV_0 - \int_{\partial \Omega_0^e \cap \partial B_{02}} \bar{\boldsymbol{T}} \cdot \boldsymbol{\varphi}_h dS_0 \right\} \\ \equiv I_h^1 - I_h^2 - I_h^3 \end{aligned} \tag{2.17}$$

Corresponding system of nodal force equilibrium equations (2.12)

$$r_{kb} = \frac{\partial I_h}{\partial x_{kb}} = \sum_{e=1}^{E} \left\{ \int_{\Omega_0^e} P_{kJ} N_{b,J} dV_0 - \int_{\Omega_0^e} \rho_0 B_k N_b dV_0 - \int_{\partial \Omega_0^e \cap \partial B_{02}} \bar{T}_k N_b dS_0 \right\} = 0$$

Next we compute the variations of each of the terms in Eq. 2.17 with respect to $\boldsymbol{X}_h$. To this end, write

$$I_h^1 = \sum_{e=1}^{E} \int_{\hat{\Omega}} W \left(\sum_{a=1}^{n} x_{ia} \hat{N}_{a,A} \frac{\partial \hat{X}_A}{\partial X_J} \right) \det(\hat{\nabla} \boldsymbol{\eta}^e) d\hat{\Omega} \tag{2.18}$$

Taking variations with respect to $\delta \boldsymbol{X}_h$ gives

$$\begin{aligned} \delta I_h^1 = \sum_{e=1}^{E} \int_{\hat{\Omega}} \Bigg\{ -P_{iJ} \left[\sum_{a=1}^{n} x_{ia} \hat{N}_{a,A} \frac{\partial \hat{X}_A}{\partial X_K} \left(\sum_{b=1}^{n} \delta X_{bK}^e \hat{N}_{b,B} \right) \frac{\partial \hat{X}_B}{\partial X_J} \right] \\ + W \left(\sum_{b=1}^{n} \delta X_{bK}^e \hat{N}_{b,B} \right) \frac{\partial \hat{X}_B}{\partial X_K} \Bigg\} \det(\hat{\nabla} \boldsymbol{\eta}^e) d\hat{\Omega} \end{aligned} \tag{2.19}$$

or

$$\delta I_h^1 = \sum_{e=1}^{E} \int_{\Omega_0^e} \left\{ (W\delta_{KJ} - F_{iK}P_{iJ}) \left(\sum_{b=1}^{n} \delta X_{bK}^e N_{b,J} \right) \right\} dV_0 \tag{2.20}$$

where in $\boldsymbol{M} = W\boldsymbol{I} - \boldsymbol{F}^T\boldsymbol{P}$ we recognize Eshelby's energy-momentum tensor[9]. Next we have

$$I_h^2 = \sum_{e=1}^{E} \int_{\hat{\Omega}} \rho_0 B_i \left(\sum_{a=1}^{n} x_{ia} \hat{N}_a \right) \det(\hat{\nabla}\boldsymbol{\eta}^e) d\hat{\Omega} \tag{2.21}$$

Taking variations we obtain

$$\delta I_h^2 = \sum_{e=1}^{E} \int_{\hat{\Omega}} \rho_0 B_i \left(\sum_{a=1}^{n} x_{ia} \hat{N}_a \right) \left(\sum_{b=1}^{n} \delta X_{bK}^e \hat{N}_{b,B} \right) \frac{\partial \hat{X}_B}{\partial X_K} \det(\hat{\nabla}\boldsymbol{\eta}^e) d\hat{\Omega} \tag{2.22}$$

or

$$\delta I_h^2 = \sum_{e=1}^{E} \int_{\hat{\Omega}} \rho_0 B_i \varphi_i \left(\sum_{b=1}^{n} \delta X_{bK}^e N_{b,K} \right) dV_0 \tag{2.23}$$

Finally we turn to the traction term. To this end, let $\bar{\boldsymbol{P}}$ be any tensor-valued function such that $\bar{P}_{iJ}N_J = \bar{T}_i$ on ∂B_{02} and $\bar{P}_{iJ}N_J = 0$ on ∂B_{01}. In practice, the function $\bar{\boldsymbol{P}}$ need only be one element deep. Then we have

$$I_h^3 = \int_{\partial B_0} \bar{P}_{iJ} N_J \varphi_i dS_0 = \int_{B_0} (\bar{P}_{iJ}\varphi_i)_{,J} \, dV_0 = \int_{B_0} (\bar{P}_{iJ}\varphi_{i,J} + \bar{P}_{iJ,J}\varphi) dV_0 \tag{2.24}$$

Each of the two terms in the last expression can now be given a treatment identical to the terms I_h^1 and I_h^2 discussed earlier. Collecting all terms, we obtain

$$\delta I_h =$$

$$\sum_{e=1}^{E} \int_{\Omega_0^e} \left\{ [W - \bar{P}_{k,L}\varphi_{k,L} - (\rho_0 B_k + \bar{P}_{kL,L})\varphi_k]\delta_{JK} - (P_{iJ} - \bar{P}_{iJ})F_{iK} \right\} \left(\sum_{b=1}^{n} \delta X_{bK}^e N_{b,J} \right) dV_0 \tag{2.25}$$

Here it may be noted that prescribed traction contributes only to those elements which are adjacent to traction boundary. The nodal configurational force equilibrium (2.13), therefore,

$$R_{Kb} = \frac{\partial I_h}{\partial X_{Kb}} =$$

$$\sum_{e=1}^{E} \int_{\Omega_0^e} \left\{ M_{KJ} + [-\bar{P}_{kL}\varphi_{k,L} - (\rho_0 B_k + \bar{P}_{kL,L})\varphi_k]\delta_{JK} + \bar{P}_{iJ}F_{iK} \right\} N_{b,J} dV_0 = 0 \tag{2.26}$$

For the linear elastic case similar derivation for nodal forces and configurational nodal forces can be given given by

$$r_{kb} = \frac{\partial I_h}{\partial u_{kb}} = \sum_{e=1}^{E} \left\{ \int_{\Omega_0^e} \sigma_{kj} N_{b,j} dV_0 - \int_{\Omega_0^e} \rho_0 B_k N_b dV_0 - \int_{\partial\Omega_0^e \cap \partial B_{02}} \bar{T}_k N_b dS_0 \right\} = 0$$

$$R_{Kb} = \frac{\partial I_h}{\partial X_{Kb}} = \sum_{e=1}^{E} \int_{\Omega_0^e} \left\{ m_{kj} + [-\bar{\sigma}_{kl} u_{k,l} - (\rho_0 B_k + \bar{\sigma}_{kl,l}) u_k] \delta_{jk} + \bar{\sigma}_{ij} u_{i,k} \right\} N_{b,j} dV_0 = 0 \quad (2.27)$$

where $\boldsymbol{m} = W\boldsymbol{I} - (\nabla \boldsymbol{u})^T \sigma$ is the Eshelby's energy momentum tensor for linear elastic case. As can be expected, configurational equilibrium involves Eshelby's energy momentum tensor, as configurational forces are related to material configuration. In the following we discuss more about Eshelby's energy momentum tensor and it's relation to forces on defects.

2.2.1 Eshelby's energy-momentum tensor

Material/configurational force can be interpreted as the force that causes motion of a 'defect' or 'singularity'. Here, defect or singularity should be interpreted in its broadest sense, for that may even include inhomogeneity. Presence of defect breaks translational symmetry of energy functional with respect to undeformed coordinates, and the corresponding stationarity conditions correspond to material force balance.

Material force($\boldsymbol{R}$) on a defect can be expressed as

$$\boldsymbol{R} = \int_S \boldsymbol{M} \cdot \boldsymbol{N} dS \quad (2.28)$$

where S is the closed surface containing the defect and M($=WI - \boldsymbol{F}^T \boldsymbol{P}$) is the Eshelby's energy-momentum tensor. However, if S does not contain a defect, the integral, Eq. 2.28, vanishes. So, for a system without defect linear momentum balance, $P_{iJ,J} + \rho_0 B_i = 0$, imply invariance of energy functional with respect to traslation in the reference configuration. However, in the discrete case, introduction of discretization breaks translational symmetry of energy functional in the reference configuration and hence nodes can be considered as the distribution of defects in this sense. Also in discrete case, nodal force equilibrium (2.12) does not imply nodal configurational equilibrium (2.13). This in turn provides additional set of equations (2.13) for the solution of undeformed coordinates(X_h).

In the presence of crack-tip, which qualifies as defect, Eq. 2.28 gives the force acting on

the crack-tip provided S encloses the crack-tip. Consider contour Γ in Figure. 2.2 which contains the tip of the crack, even though the crack may pass out of contour Γ, and part of the crack which lies inside Γ is straight and is parallel to X_1. Then the X_1 material force component with linearized kinematics can be given 'as

$$\boldsymbol{R^c} = \int_{\Gamma} [\boldsymbol{W^e n_1} - \boldsymbol{u_{,1}} \cdot (\boldsymbol{\sigma} \cdot \boldsymbol{n})] \boldsymbol{d\Gamma} \tag{2.29}$$

where n_1 is the X_1 component of outward normal to contour Γ, with no forces acting on the crack-tip. In the absence of body forces, R^c is path independent [5], and is known as Rice's J-integral. Further, Eshelby [10, 11] and Rice [6] have shown that J-integral can be interpreted as the energy-release rate, i.e., reduction of potential energy per unit crack extension

$$J = -\frac{\partial I}{\partial a} \tag{2.30}$$

where a is the crack length.

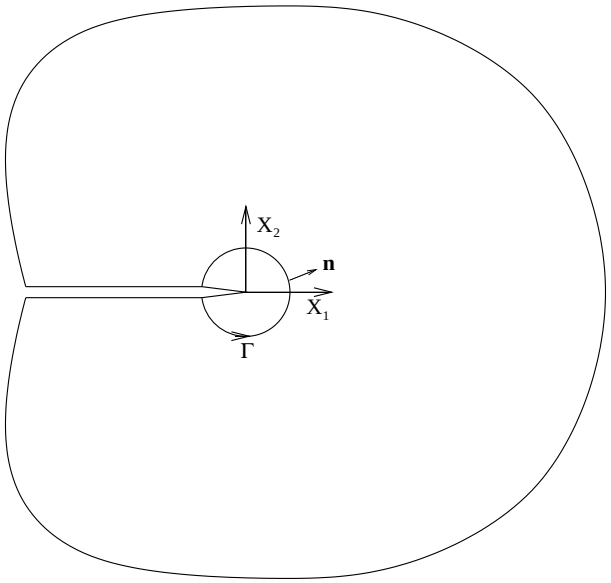

Figure 2.2: Contour for J-integral

2.2.2 Solution scheme

To obtain solution for deformed and undeformed coordinates we modified the conjugate-gradient (Polak-Rebiere version)[12] method for minimization of energy function. This

solution scheme has two levels, in which outer level is the undeformed coordinate iterative update or nodal coordinate update. Nodal coordinate iterative loop contains solution for equilibrium solution for deformed coordinate for a fixed mesh as shown in the Figure. 2.3. This guarantees that configurational forces for undeformed coordinate update correspond to equilibrium solution, which in turn guarantees positive Jacobian of the elements.

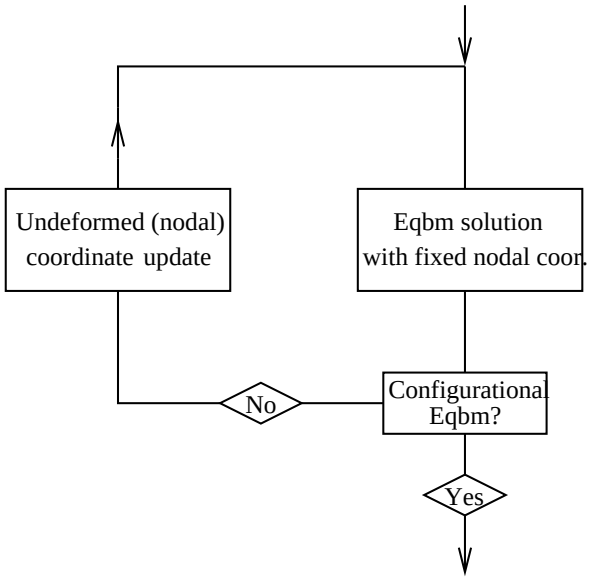

Figure 2.3: Schematic of solution scheme

Further, we used occasional re-triangulation for faster convergence. This re-triangulation is achieved by keeping nodal locations fixed but seeking new connectivity by recourse to Delaunay triangulation. This would improve mesh quality because Delaunay triangulation guarantees maximum-minimum interior angle of elements of all the possible meshes for a given point set. Good quality of the triangulation so obtained provides faster convergence i.e., needs few iterations to converge. It is important to note that for the problems involving internal (state) variables, recourse to re-triangulation necessitates mesh-to-mesh transfer, and is undesirable.

2.3 Numerical tests

In this section, we report the results of number of numerical tests which establish the effectiveness of this method of mesh adaption.

2.3.1 Elastic rod under uniform body force

In this section we present results for 1-D linear-elastic rod which is under uniform body force b as shown in Fig. 2.4 with one end fixed and the other end free. The displacement

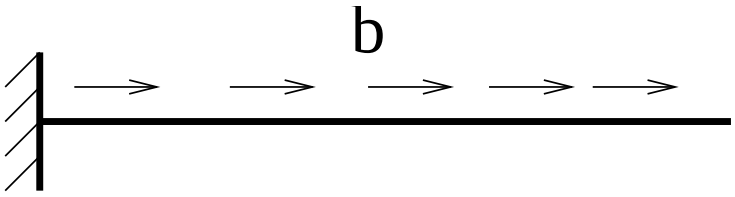

Figure 2.4: Geometry of 1-D rod under uniform body force

solution for this problem can be given as:

$$u(X) = \frac{b}{E}(X - \frac{X^2}{2}) \tag{2.31}$$

where E is the elastic modulus of the material. Here for simplicity we chose $E = 1$ and $b = 1$. Corresponding to this displacement, strain and stress are linear in X. This suggests that uniform mesh is the optimal mesh corresponding to this solution. To verify the ability of VALE to recover the optimal mesh we begin by meshing the domain with the initial mesh shown in Fig. 2.5(a). In this mesh, but for the node at the free end, all other nodes are clustered at the fixed end (node at the free end is necessary to define the geometry). Following mesh adaption we obtain uniform mesh (Fig. 2.5(b)) as expected. In this figure, analytic solution is superposed on the numerical for the purpose of comparison.

2.3.2 Mode-I crack problem

Here we conducted convergence studies for linear-elastic isotropic (2.32), plain strain, mode-I crack problem. We consider both 2-D and 3-D cases with prescribed K_I field on the boundary as shown in Fig. 2.6. Constitutive law for the linear-elastic material is given by Hooke's law

$$\sigma_{ij} = \lambda \delta_{ij} u_{k,k} + \mu(u_{i,j} + u_{j,i}) \tag{2.32}$$

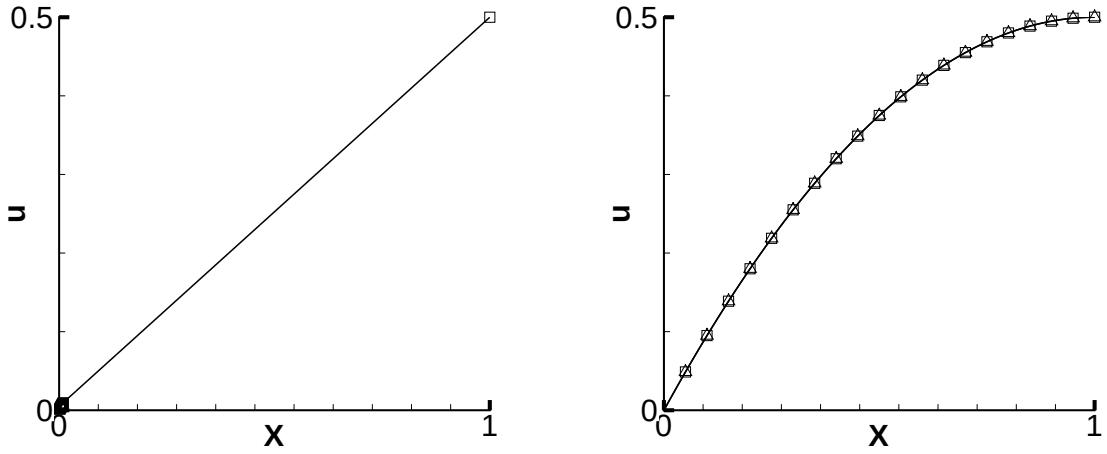

(a) (b)

Figure 2.5: Evolution of mesh: a) Initial mesh; b) Optimum uniform mesh

where λ and μ are the elastic constants. For the particular choice of material chosen here, elastic constants are given by

$$\lambda_0 = 125.48\ MPa$$
$$\mu_0 = 83.65\ MPa$$

This problem is chosen because analytic solution [25] is known for this problem, which in turn enables convergence analysis with and without mesh adaption. Further, corresponding analytical solution has singularity at the crack tip, which demonstrates the robustness of the present adaption scheme in resolving steep gradients. Following are the analytic expressions for displacements

$$\begin{aligned} u_1 &= \frac{K_I}{2\mu}\sqrt{\frac{r}{2\Pi}}\left[2 - 4\nu + 2\sin^2(\frac{\theta}{2})\right] \\ u_2 &= \frac{K_I}{2\mu}\sqrt{\frac{r}{2\Pi}}\left[4 - 4\nu - 2\cos^2(\frac{\theta}{2})\right] \\ u_3 &= 0 \end{aligned} \tag{2.33}$$

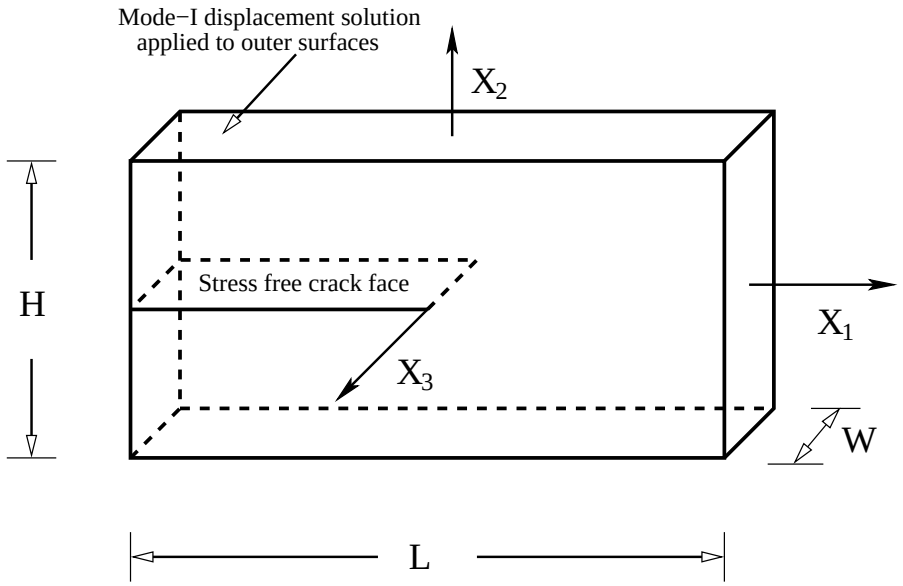

Figure 2.6: Geometry of the mode-I fracture problem considered in the convergence study

and for stresses

$$\begin{aligned}
\sigma_{11} &= \frac{K_I}{\sqrt{(2\pi r)}}\cos(\frac{\theta}{2})\left[1-\sin(\frac{\theta}{2})\cos(\frac{3\theta}{2})\right] \\
\sigma_{22} &= \frac{K_I}{2\pi r}\cos(\frac{\theta}{2})\left[1+\sin(\frac{\theta}{2})\cos(\frac{3\theta}{2})\right] \\
\sigma_{12} &= \frac{K_I}{2\pi r}\cos(\frac{\theta}{2})\sin(\frac{\theta}{2})\cos(\frac{3\theta}{2}) \\
\sigma_{33} &= \frac{2\nu K_I}{2\pi r}\cos(\frac{\theta}{2}) \\
\sigma 13 &= 0 \\
\sigma 23 &= 0
\end{aligned} \tag{2.34}$$

where K_I is the stress intensity factor, r and θ are the polar coordinates in X_1-X_2 plane. In this section, analysis has been performed with mode-I stress intensity factor of

$$K_I = 1.0MPa\sqrt{m}$$

The following norms and semi-norms are used to quantify solution errors and gauge the

performance of this mesh adaption scheme:

$$\|\boldsymbol{u}\|_0 = \left\{\int_\Omega |\boldsymbol{u}|^2 d\Omega\right\}^{1/2} \tag{2.35}$$

$$|\boldsymbol{u}|_E = \left\{\int_\Omega \sigma_{ij} u_{i,j} d\Omega\right\}^{1/2} \tag{2.36}$$

$$\tag{2.37}$$

where $\boldsymbol{u}$ and $\boldsymbol{\sigma}$ are the displacement vector and stress tensor, respectively. Evidently, $\|\boldsymbol{u}\|_0$ is the L_2 norm of $\boldsymbol{u}$, whereas $|\boldsymbol{u}|_E$ is the energy semi-norm.

2.3.2.1 Two-dimensional linear elastic crack

In this section, we present results of 2-D computations for a mode-I plane strain problem. Owing to the symmetry, only upper half of the geometry is modeled with appropriate symmetry boundary conditions. Typical initial mesh used for the numerical computation is given in Fig. 2.7(a). This mesh consists of linear triangle elements with uniform mesh size. For modeling mode-I crack, we prescribe the displacement field corresponding to the mode-I crack (2.33) on the faces, facing away from the crack-tip, Fig. 2.6. Further, to model symmetry, nodes on the face ahead of the crack-tip are prescribed with zero X_2 component of the displacement, i.e., $u_2 = 0$. Since nodal coordinates are also sought as the solution, we need to prescribe appropriate boundary conditions for undeformed coordinate to maintain the geometry in reference configuration. In the present case appropriate boundary conditions for undeformed coordinates are such that the nodes on the faces with normals along X_1 direction are allowed to move only in X_2 direction, i.e, prescribed X_1 component of undeformed coordinate, and vice versa. With these boundary conditions we performed numerical computations for several meshes with different initial mesh sizes. Fig. 2.7 shows one such result, wherein beginning with a uniform mesh we obtain optimal mesh focused at the crack-tip, as a consequence of nodal flow towards the crack-tip. This is to be expected as singularity ($\mathrm{O}(\frac{1}{\sqrt{r}})$) (2.34) is located at the crack-tip and where gradients are steep. In this particular case area of the element ahead of crack-tip after mesh adaption is $\frac{1}{200}^{th}$ that of the same element before mesh adaption. It is worth emphasizing that this mesh adaption has been accomplished without error estimation and mesh-to-mesh transfer.

The solution so obtained satisfies nodal configurational equilibrium (2.13) in addition

to nodal force equilibrium (2.12). For the nodes on the faces with prescribed K_I the corresponding configurational equilibrium equations are provided by Eq. 2.15.

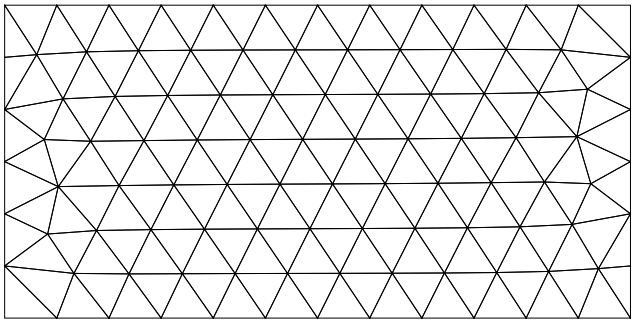

(a)

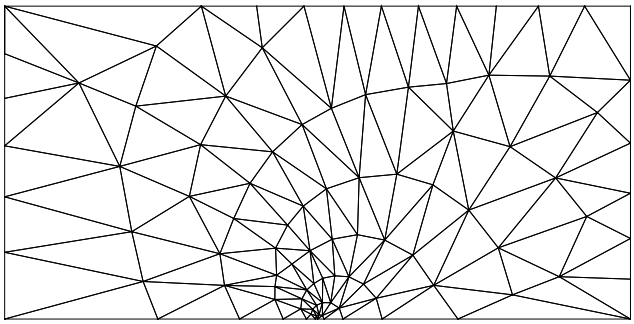

(b)

Figure 2.7: Two-dimensional analysis of a semi-infinite crack in a linear elastic solid subject to mode-I loading. The initial computational mesh consists of 166 three-node triangular elements. Evolution of mesh: a)Initial uniform mesh; b)Optimal mesh focused at the crack tip

Fig. 2.8 shows dependence of normalized displacement error norm and energy error semi-norm on mesh size (h) (here mesh size is element size of the initial uniform mesh). The error norms are normalized by the corresponding norm of the exact field (2.33, 2.34). The convergence rates deduced from these plots are collected in Table 2.1. The convergence rate is the slope of the error vs. mesh size curve in the logarithmic axes.

Following are some of the observations based on these numerical results:

- Here, it can be observed that the solution corresponding to the optimal mesh is more accurate. This is to be expected as the numerical solution, 'stiff solution', is bounded below by the exact solution.

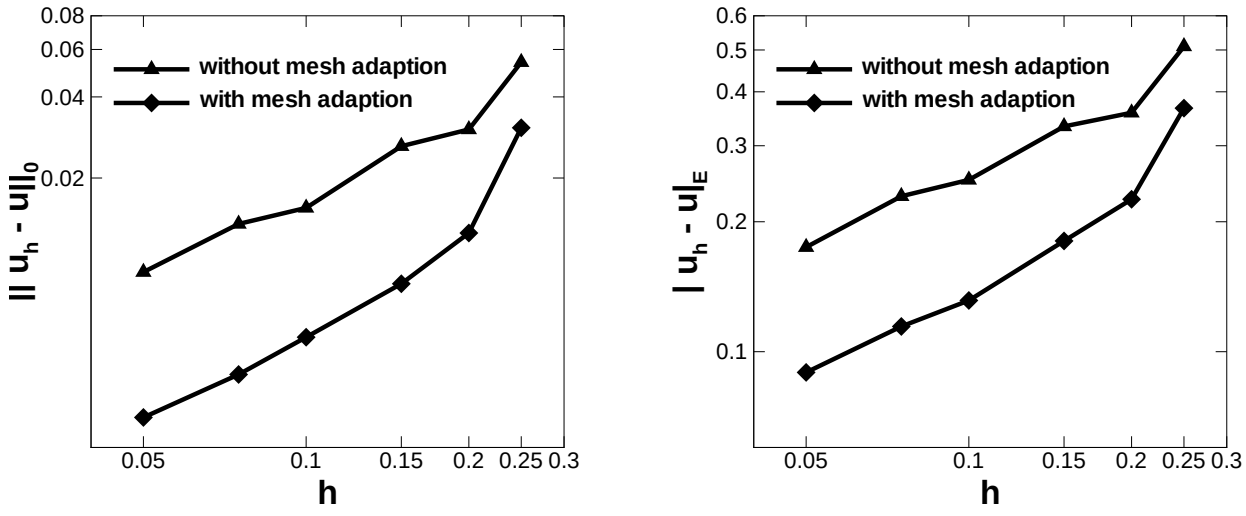

(a) (b)

Figure 2.8: Two-dimensional analysis of a semi-inifinite crack in a linear elastic solid subjected to mode-I loading , convergence plots: a) L_2-norm of displacement error; b) Energy norm of displacement error.

- Mesh adaption not only reduces error, but also improves rate at which solution converges to exact solution, Table 2.1. Inspite of presence of strong singularities we recover optimal convergence rate while the uniform refinement gives sub-optimal convergence.

- Since we seek solution for the nodal coordinates, the size of the solution array is twice as much when compared to the solution without mesh adaption. However, as can be seen from the Fig. 2.8, gain in accuracy is more than offsets increase in solution array size. In particular consider case with mesh size $h = 0.15$ for which both error norms after mesh adaption are less than that of the errors for uniform mesh, i.e., without mesh adaption, for the mesh with size $h = 0.05$ even though in latter case solution array size is 4.5 (0.5×3^2) times than that in the former case.

2.3.2.2 J-integral

In fracture mechanics J-integral [5] is one of the most important parameters and is a measure of strength of singular fields at crack-tip. One of the important properties of J-integral is

	$\| \boldsymbol{u}_h - \boldsymbol{u} \|_0$	$\|\boldsymbol{u}_h - \boldsymbol{u}\|_E$
without mesh adaption	0.8794	0.5172
with mesh adaption	1.1369	0.6662

Table 2.1: Convergence rates for two-dimensional analysis of a semi-infinite crack in a linear elastic solid subjected to mode-I loading.

that it is a measure of strength of crack-tip field singularity (HRR fields) and is path independent in the absence of crack face traction. It is defined as the energy release rate per unit crack extension and is the configurational (material) force component along crack face tangential direction, in this case X_1-direction, of the crack-tip node ($\boldsymbol{X}0$) [4] and is given by

$$J = -\frac{\partial I_h}{\partial X 0_1} \tag{2.38}$$

In the present method, J-integral evaluation is point-wise at crack-tip node which is in

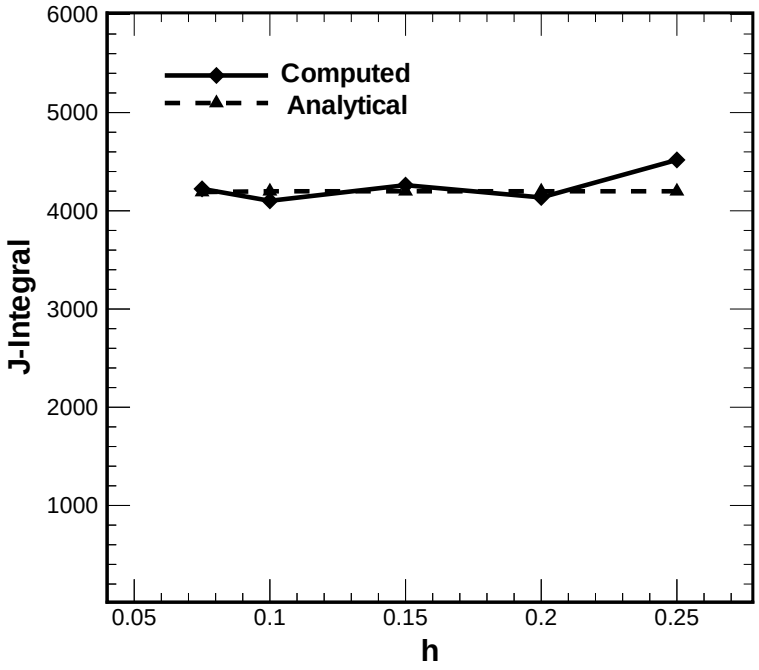

Figure 2.9: J-integral variation with mesh size

contrast to traditional methods, where it is evaluated by recourse to either contour integral [5] or domain integral evaluation [7, 8]. Further, this method of J-integral evaluation is very

accurate as can be seen in Fig. 2.9, in which but for the coarsest mesh all other meshes give J-integral within 2.5% of the analytical $J(=\frac{(1-\nu^2)K_I^2}{E})$. This is very impressive considering that J-integral has been evaluated corresponding to the node which is located right at singularity. This accuracy can be attributed to the ability of this method of mesh adaption to resolve steep gradients. In addition, this method does not need interpolation unlike in the case of contour integral method, where we need to interpolate stresses and strains onto contour for the evaluation of contour integral. For the case when body forces are present, traditional way of J-integral evaluation requires domain integral evaluation right up to crack tip, which in addition to being computationally expensive is also inaccurate. However the present method provides good computational accuracy even in the presence of body forces and also computational cost is independent of presence of body forces.

2.3.2.3 Three-dimensional linear elastic crack

The performance of the method in three dimensions is illustrated next. To this end we present the results of 3-D computations for a mode-I plane strain problem. Owing to the symmetry, as in the 2-D case, only upper half of the geometry is modeled with appropriate symmetry boundary conditions. Further lateral faces, faces perpendicular to X_3 axis, are prescribed with boundary condition $u_3 = 0$, so as to model plain strain condition. Here, as before, we prescribe displacement boundary conditions corresponding to K_I-field (2.33) on the faces, facing away from the crack front, Fig. 2.6. To maintain geometry we prescribe appropriate boundary conditions for X_1 component on the faces with normal along X_1 axis, X_2 component on the faces with normal along X_2 and X_3 component on the faces with normal along X_3. With these boundary conditions analysis has been performed for different mesh sizes with initial uniform mesh. This mesh consists of linear tetrahedral elements. Fig. 2.10 shows one such mesh before and after mesh adaption. As can be expected mesh adaption provides fine mesh along crack-front. This is to be expected as singularity is located along the crack-front and where gradients are steep. The resulting optimal mesh satisfies nodal configurational force equilibrium (2.12). Fig. 2.11 shows dependence of normalized displacement error norm and energy error semi-norm on mesh size (h). As in 2-D case mesh adaption in addition to reducing error, Fig. 2.11, also improves convergence rates, Table 2.2. Here again similar observations, as in the case of 2-D, can be made.

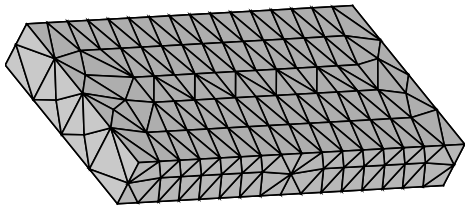

(a)

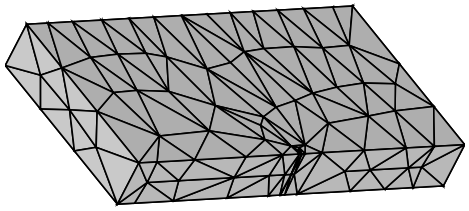

(b)

Figure 2.10: Three dimensional analysis of a semi-infinite crack in a linear elastic solid subjected to mode-I loading. The initial computational mesh consists of 493 four-node tetrahedral elements: a) Initial uniform mesh ; b) Optimal mesh focused at the crack tip.

2.3.3 Neo-hookean solid under moving point load

In previous examples, linearized kinematics has been assumed. In this section performance of this method for the case of finite kinematics has been demonstrated. To this end, method has been applied for the case of Neo-hookean solid subjected to moving point load under plain strain condition. For this purpose we chose rectangle block with 10 m width and 5 m height, which is supported at the bottom and anchored at one end, and is shown in Fig. 2.12. Corresponding strain energy density function W, for Neo-hookean solid extended

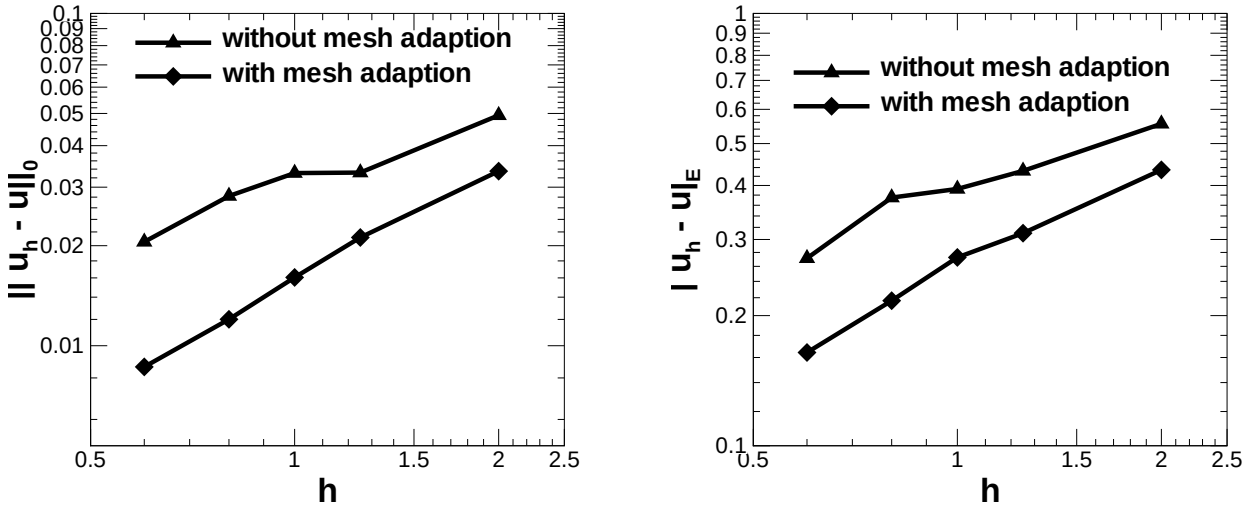

(a) (b)

Figure 2.11: Three-dimensional analysis of a semi-infinite crack in a linear elastic solid subjected to mide-I loading: a) L_2-norm of displacement error; b) Energy norm of displacement error.

	$\| \boldsymbol{u}_h - \boldsymbol{u} \|_0$	$\|\boldsymbol{u}_h - \boldsymbol{u}\|_E$
without mesh adaption	0.728	0.58485
with mesh adaption	1.12653	0.80787

Table 2.2: Three-dimensional analysis of a semi-infinite crack in a linear elastic solid subjected to mode-I loading, convergence rates

to the compressible range, is given as follows

$$W(\boldsymbol{F}) = \frac{1}{2}\lambda_0(\log J)^2 - \mu_0 \log J + \frac{\mu_0}{2}\mathrm{tr}(\boldsymbol{F}^T\boldsymbol{F}) \tag{2.39}$$

where λ_0 and μ_0 are material constants and $J = det(\boldsymbol{F})$. The corresponding stress-strain relationship is

$$\boldsymbol{P} = \lambda_0 \log J \boldsymbol{F}^{-T} + \mu_0(\boldsymbol{F} - \boldsymbol{F}^{-T}) \tag{2.40}$$

The material chosen here is steel for which material constants are given by

$$\lambda_0 = 115.4\ GPa$$

$$\mu_0 = 76.9\ GPa$$

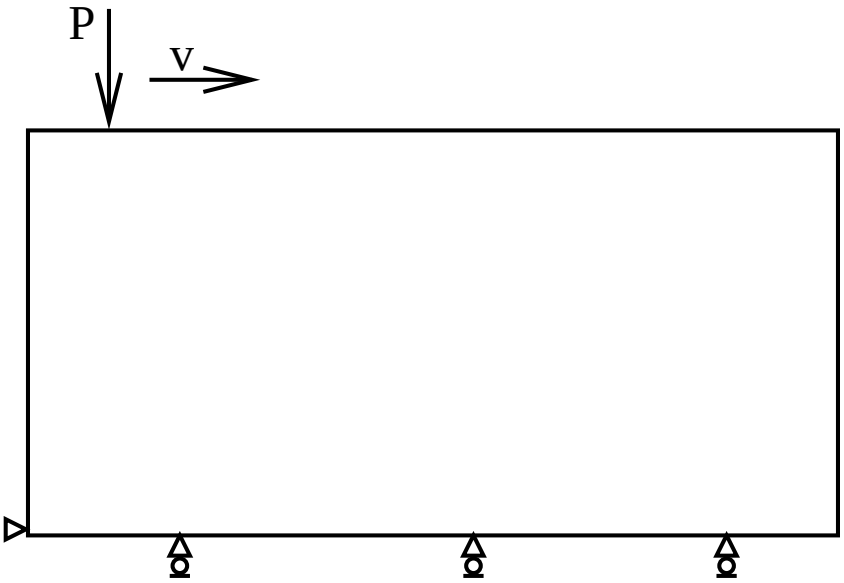

Figure 2.12: Schematic of neohookean solid subject to moving load

Fig. 2.13 shows initial mesh chosen for the numerical computations. This mesh consists of linear triangle elements with uniform mesh size. For the computations we prescribe zero vertical deformation for the bottom face and zero horizontal deformation for node at the left corner. As before, appropriate boundary conditions for undeformed coordinates have been prescribed for the boundary nodes so as to maintain the geometry during mesh adaption. Computations have been performed for the moving point load. Fig. 2.14 shows vertical displacement contours for four such positions of point load. As can be observed after mesh adaption, nodes are focused at the point of application of load due to the presence of steep gradients since in linear elastic solution for the similar case of point load on elastic half space, stress and strain solution has $O(\frac{1}{r})$ singularity [48].

2.4 Summary and conclusions

We have developed a novel method 'VALE', in which in addition to nodal variables mesh itself is sought as solution by solving for nodal (undeformed) coordinates. Further we have analyzed one of its most important applications as a mesh adaption scheme. The resulting mesh adaption scheme has the following advantages :

1. It is variationally consistent and based on sound principles. In addition, it provides precise criterion for optimal mesh (nodal configurational equilibrium). The optimal

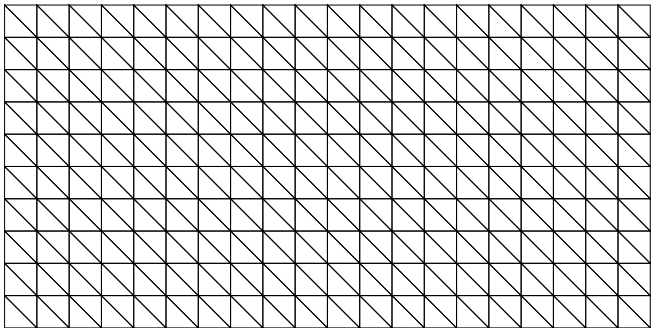

Figure 2.13: Initial uniform mesh of the computational domain of neohookean solid subject to moving point load

mesh so obtained provides the most accurate solution for a given number of nodes.

2. Does not involve error estimation.

3. Does not involve mesh-to-mesh transfer and hence is devoid of associated interpolation errors.

4. In this scheme, only nodal coordinates change and everything else remains same. This in turn obviates mesh remapping onto processors in parallel mesh adaption and hence ideally suited for parallel computation.

Since mesh itself is the solution, it is ideal for the solution of reference configuration as in the case of shape optimization. Also, the number of nodes and elements remains the same as in the initial mesh, which provides complete control over the size of the problem and yet provides the most accurate solution possible. However one can refine mesh, by simply adding nodes to the mesh, for example, at the centroid of any of the existing elements and the resulting refinement scheme is completely local.

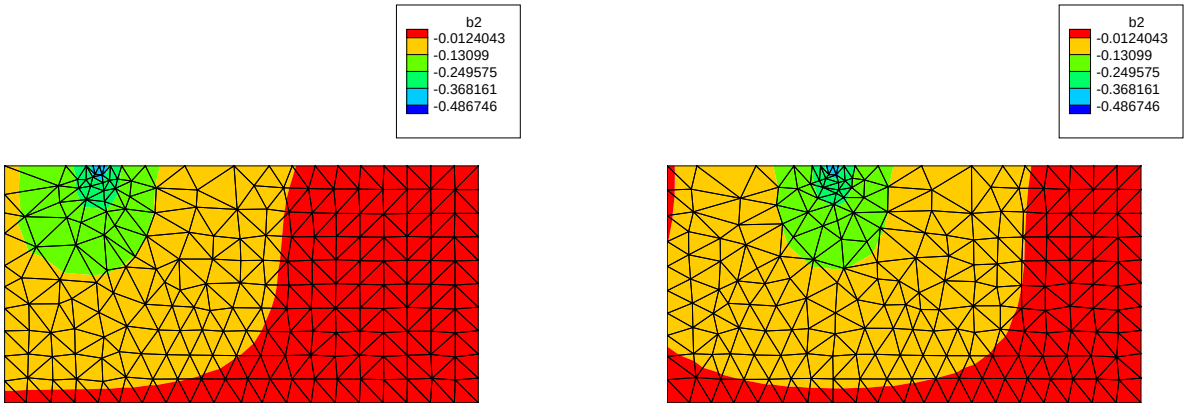

(a)

(b)

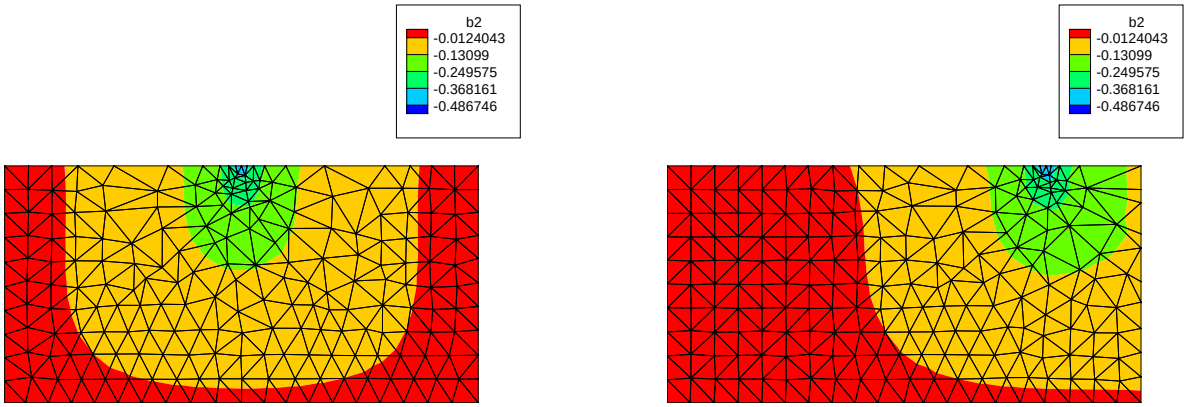

(c)

(d)

Figure 2.14: vertical displacement contours for the point load locations.

Chapter 3

Shape optimization

3.1 Introduction

In engineering applications shape optimization plays a very important role. These applications involve determination of structure-property relationships and optimal design of structures. To accomplish this, several numerical schemes have been developed most of which include seeking solution for material distribution [35, 36, 50], which in turn cannot provide sharp interfaces, when it does, it causes checker board formation. However, the method developed by Jog et al. [18], which is similar to the method described in this chapter, seeks solution by solving for interface nodal coordinates and hence retains sharp material interface but has restriction of linearized kinematics.

In this chapter, we present a method which has no restrictions on either the constitutive behavior of the material or the kinematics. This can be accomplished in a natural manner when accounting for horizontal variations, for it allows the solution of shape by seeking solution for undeformed (nodal) coordinates of the boundary and/or interfaces. In this chapter we consider one such important application, wherein the equilibrium shapes of coherent, misfitting inclusions are obtained.

The concept of 'equilibrium shape' provides a simple criterion for understanding particle shapes and their evolution during precipitation. In such an approach, the particle is assumed to take a shape which minimizes an appropriate energy of the system under volume constraint. In this chapter we study equilibrium shape of an isolated, coherent precipitate with dilatational misfit.

3.2 Variational formulation

Consider two precipitate geometries of the same mass (same volume in reference configuration), but with different inclusion shapes, as shown in the Fig. 3.1. (It should be mentioned that these are two different material configurations and are not obtained as a consequence of superimposing displacement on the reference configuration.) Equilibrium solutions obtained for these two material configurations are different. So, for such inhomogeneous system energy function also depends on material configuration is addition to boundary conditions and geometry. In statics, minimum energy principle suggests that natural configuration for such inhomogeneous system is the one corresponding to the configuration, which has minimum energy amongst all the possible material configurations satisfying volume constraint and with the same boundary conditions. In this section, we develop variational formulation for finding the natural material confgiuration corresponding to the optimal shape of the inclusion. In particular we consider the following model problem. For a given misfit strain and

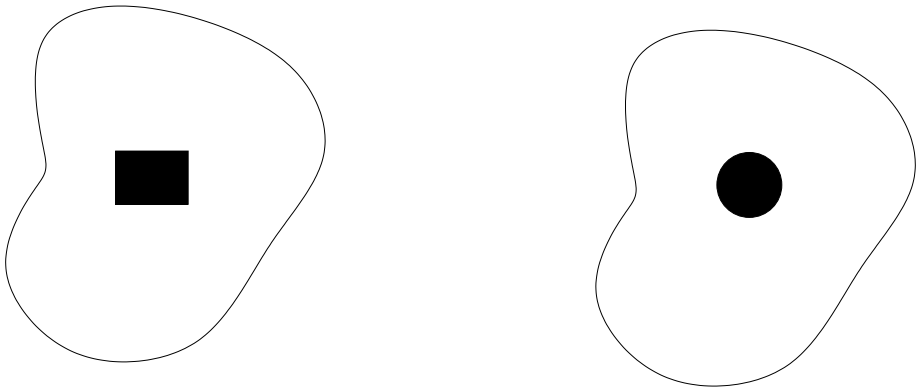

Figure 3.1: Different shapes of inclusion

interface energy, find the equilibrium shape, which has minimum total energy in the matrix, inclusion and interface, subject to the constraint that the volume of the inclusion remains constant. The reason for specific choice of problem is the interesting bifurcation phenomena associated with dilatational misfit case and availability of the analytical solution.

Let $B_0 = B_{01} \cup B_{02}$ denote the total domain which is composed of matrix B_{01} and inclusion B_{02} with the interface ∂B_{02}. Appropriate energy for the minimum principle for

this system is

$$I = \int_{B_0} W(\nabla_0 \boldsymbol{\varphi}) dV_0 + \int_{\partial B_{02}} \gamma dS_0 + \frac{1}{2}\alpha(A_0 - \int_{B_{02}} dV_0)^2 \tag{3.1}$$

where W is the strain energy density, γ is the interface energy density for interface, ∂B_{02} interface area, A_0 initial second phase particle volume. Here, penalty method has been chosen for imposing volumetric constraint, and α is the associated penalty parameter. The functional is discretized by the introduction of a finite-element interpolation of the form as before:

$$\boldsymbol{\varphi}_h(\boldsymbol{X}) = \sum_{a=1}^{N} \boldsymbol{x}_a N_a(\boldsymbol{X}) = \sum_{a=1}^{n} \boldsymbol{x}_a^e N_a^e(\boldsymbol{X}), \boldsymbol{X} \in \Omega^e \tag{3.2}$$

where $E = E_m + E_p$, E_m and E_p are the number of matrix and inclusion elements, respectively, N total number of nodes in the mesh and n number of nodes per element. Elements adjacent to interface are such that one of their edges, faces in the 3-D case, are aligned with the interface i.e., material interface does not cut across any of the element. So, each element is uniquely identified with one of the material and this identification remains the same during the computations. Essentially, interface is defined with a set of edges or faces connected by the nodes. So, finding optimal shape corresponds to finding optimal nodal locations, for the nodes on the interface, corresponding to minimum energy and with fixed edge or face connectivity.

As before we further restrict attention to isoparametric element and consider element shape functions are of the form:

$$N_a^e = \hat{N}_a^e \circ \boldsymbol{\eta}^{e-1} \tag{3.3}$$

where

$$\boldsymbol{\eta}^e(\hat{\boldsymbol{X}}) = \sum_{a=1}^{n} \boldsymbol{X}_a \hat{N}_a(\hat{\boldsymbol{X}}) \tag{3.4}$$

is the isoparametric mapping for element e, defined over the standard domain $\hat{\Omega}$ of the element. Then the discretized energy function:

$$I_h = \int_{B_0} W(\nabla_0 \boldsymbol{\varphi}_h) dV_0 + \int_{\partial B_{02}} \gamma dS_0 + \frac{1}{2}\alpha(A_0 - \int_{B_2} dV_0)^2 \tag{3.5}$$

may now be regarded as a function of the nodal coordinates $\boldsymbol{x}_h \equiv \{\boldsymbol{x}_a, a = 1, \ldots, N\}$ and $\boldsymbol{X}_h \equiv \{\boldsymbol{X}_a, a = 1, \ldots, N\}$ in the deformed and undeformed configurations, respectively.

To obtain equilibrium shape, we minimize I_h with respect to $\{\boldsymbol{x}_h, \boldsymbol{X}_h\}$. Strictly speaking, optimal shape is provided by the minimum with respect to nodes on the interfaces. However, minimization with respect to other nodes provides mesh adaption and enables efficient shape optimization. The corresponding stationarity condition corresponding to the minima:

$$\langle DI_h, \delta\boldsymbol{x}_h\rangle \cdot \delta\boldsymbol{x}_h + \langle DI_h, \delta\boldsymbol{X}_h\rangle \cdot \delta\boldsymbol{X}_h = 0 \tag{3.6}$$

and since $\delta\boldsymbol{x}_h$ and $\delta\boldsymbol{X}_h$ are independent, except on Dirichlet boundary, we have the following conditions

$$\langle DI_h, \delta\boldsymbol{x}_h\rangle = 0 \tag{3.7}$$

$$\langle DI_h, \delta\boldsymbol{X}_h\rangle = 0 \tag{3.8}$$

which enforce equilibrium of nodal forces and configurational nodal forces, respectively.

In order to further explicate the stationarity conditions we begin by expressing the discretized energy in the form:

$$I_h = \sum_{e=1}^{E} \int_{\Omega_0^e} W(\nabla_0 \boldsymbol{\varphi}_h) dV_0 + \int_{\partial B_{02}} \gamma dS_0 + \frac{1}{2}\alpha(A_0 - \int_{\Omega_0^e} dV_0)^2$$

$$\equiv I_h^1 + I_h^2 + I_h^2 \tag{3.9}$$

More explicitly nodal force equilibrium equations are

$$r_{bk} = \frac{\partial I_h}{\partial x_{bk}} = \frac{\partial I_h^1}{\partial x_{bk}} \sum_{e=1}^{E} \int_{\Omega_0^e} P_{bJ} N_{k,J} dV_0 \tag{3.10}$$

Next we compute the variations of each of the terms $(I_h^i, i = [1,3])$ with respect to $\boldsymbol{X}_h$. To this end, write

$$I_h^1 = \sum_{e=1}^{E} \int_{\hat{\Omega}} W \left(\sum_{a=1}^{n} x_{ia} \hat{N}_{a,A} \frac{\partial \hat{X}_A}{\partial X_J} \right) \det(\hat{\nabla}\boldsymbol{\eta}^e) d\hat{\Omega} \tag{3.11}$$

Taking variations with respect to $\delta\boldsymbol{X}_h$ gives

$$\delta I_h^1 = \sum_{e=1}^{E} \int_{\hat{\Omega}} \left\{ -P_{iJ} \left[\sum_{a=1}^{n} x_{ia} \hat{N}_{a,A} \frac{\partial \hat{X}_A}{\partial X_K} \left(\sum_{b=1}^{n} \delta X_{bK}^e \hat{N}_{b,B} \right) \frac{\partial \hat{X}_B}{\partial X_J} \right] \right.$$

$$+W\left(\sum_{b=1}^{n}\delta X_{bK}^{e}\hat{N}_{b,B}\right)\frac{\partial\hat{X}_B}{\partial X_K}\Bigg\}\det(\hat{\nabla}\boldsymbol{\eta}^e)d\hat{\Omega} \tag{3.12}$$

or

$$\delta I_h^1=\sum_{e=1}^{E}\int_{\Omega_0^e}\left\{(W\delta_{KJ}-F_{iK}P_{iJ})\left(\sum_{b=1}^{n}\delta X_{bK}^{e}N_{b,J}\right)\right\}dV_0 \tag{3.13}$$

where in $W\boldsymbol{I}-\boldsymbol{F}^T\boldsymbol{P}$ we recognize Eshelby's energy-momentum tensor. Next we have

$$I_h^2=\sum_{e=1}^{S_i}\int_{\partial\hat{\Omega}}|\boldsymbol{r}_{,\xi_1}\times\boldsymbol{r}_{,\xi_2}|d\xi_1 d\xi_2 \tag{3.14}$$

for 3-D case where $\boldsymbol{r}$ is the position vector of points on the surface, which can be obtained by isoparametric interpolation of nodes on the surface, ξ_1 and ξ_2 are parameters of parametric representation of the surface and S_i is the number of surface elements associated with the interface.

Taking variations we obtain

$$\delta I_h^2=\sum_{e=1}^{S_i}\int_{\partial\hat{\Omega}}\frac{(\boldsymbol{r}_{,\xi_1}\times\boldsymbol{r}_{,\xi_2})_I}{|\boldsymbol{r}_{,\xi_1}\times\boldsymbol{r}_{,\xi_2}|}[\epsilon_{IKM}((\boldsymbol{r}_{,\xi_2})_M N_{b,\xi_1}-(\boldsymbol{r}_{,\xi_1})_M N_{b,\xi_2})]\delta X_{bK}^{e}d\xi_1 d\xi_2 \tag{3.15}$$

similarly for 2-D case we have

$$I_h^2=\sum_{e=1}^{S_i}\int_{\partial\hat{\Omega}}|\boldsymbol{r}_{,\xi}|d\xi \tag{3.16}$$

here we have one parameter ξ. Taking variations we obtain

$$\delta I_h^2=\sum_{e=1}^{S_i}\int_{\partial\hat{\Omega}}\frac{(\boldsymbol{r}_{,\xi})_K}{|\boldsymbol{r}_{,\xi}|}N_{b,\xi}\delta X_{bK}^{e}d\xi \tag{3.17}$$

and taking variations of the last term we obtain

$$\delta I_h^3=-\alpha(A_0-\sum_{e=1}^{E_p}\int_{\Omega_0^e}dV_0)\sum_{e=1}^{E_p}\int_{\Omega_0^e}(\sum_{b=1}^{n}\delta X_{bK}^{e}N_{b,K})dV_0 \tag{3.18}$$

collecting all terms we obtain

$$\delta I_h=R_{bK}\delta X_{bK} \tag{3.19}$$

where R_{bK} are nodal configurational forces corresponding to the configurational equilibrium

equations

$$R_{bK} = 0 \tag{3.20}$$

The nodal configurational force equilibrium not only provides optimal mesh but also provides equilibrium shape of the inclusion. This can be explained by the fact in the non-homogeneous case, even in the continuous case, energy functional does not possess translational symmetry in reference configuration even in the continuous case. In contrast, in homogeneous case introduction of discretization breaks translational symmetry in the reference configuration even though in the continuous case energy functional possesses translational symmetry in reference configuration. To explain this consider inhomogeneous case with $W(\boldsymbol{F}(\boldsymbol{X}), \boldsymbol{X})$, continuous in X, for which the energy can be expressed as

$$I = \int_{B_0} W(\boldsymbol{F}(\boldsymbol{X}), \boldsymbol{X}) dV_0 \tag{3.21}$$

Euler-Lagrange equations corresponding to variations in deformed coordinates are

$$\nabla_0 \cdot \boldsymbol{P} = 0 \tag{3.22}$$

which are force equilibrium equations. Similarly Euler-Lagrange equations corresponding to variations in undeformed coordinates are [14]:

$$\frac{\partial W}{\partial \boldsymbol{X}} - \nabla_0 \cdot \boldsymbol{M} = 0 \tag{3.23}$$

which are configurational force equilibrium equations. Eq. 3.22 does not imply translation invariance of energy functional with respect to translation in reference configuration. However, when $W(\boldsymbol{F})$ does not explicitly depend on $\boldsymbol{X}$ ($\frac{\partial W}{\partial \boldsymbol{X}} = 0$), i.e., homogeneous case, Eq. 3.22 imply translation invariance of energy functional with respect to traslations in reference configuration.

3.3 Numerical test

In this section we present results for a system in which an isolated inclusion is coherently embedded in a matrix of infinite extent and in the presence of surface energy. Further both

inclusion and matrix are of linear elastic material with different elastic constants (3.24).

$$\begin{aligned} \sigma = \mathbf{C_2} : (\epsilon - \epsilon^*_\mathbf{i}) \quad &: \quad \text{inclusion} \\ \sigma = \mathbf{C_1} : (\epsilon - \epsilon^*_\mathbf{m}) \quad &: \quad \text{matrix} \end{aligned} \tag{3.24}$$

where $\mathbf{C_1}$ and $\mathbf{C_2}$ are the elasticity tensors for matrix and inclusion, respectively, and $\epsilon^*_\mathbf{i}$ and $\epsilon^*_\mathbf{m}$ are transformational strains for the inclusion and matrix, respectively. Further we consider problem with dilatational misfit, i.e., $\epsilon^*_\mathbf{i}$ is dilatational and $\epsilon^*_\mathbf{m} = \mathbf{0}$. Here we consider both isotropic and orthotropic cases.

3.3.1 Isotropic-dilatation misfit case

In this section we consider a linear-elastic isotropic system with different dilatational transformational strains for matrix and inclusion. In particular, Johnson and Cahn [15] have studied the case with zero transformational strain for the matrix, analytically. In this case elastic strain energy, corresponding to first term in Eq. 3.1, scales with inclusion volume and favors elliptic geometry of the inclusion [19]. However surface energy scales with interface area and favors circular geometry of the inclusion. So, actual shape of the inclusion is dependent on the size of the inclusion. Specifically, for small inclusion sizes, the surface to volume ratio is such that the particle shapes will be dominated by the interfacial energy, which in turn favors circular shape, while in the large-inclusion-size limit, the elastic terms will dominate, which in turn favors elliptic shape. This suggests a critical length scale r^* (since there is one order difference in dependencies, i.e., volume/surface area ratio) associated with this shape transition and the associated phenomena is called 'symmetry-breaking shape transition' by Johnson and Cahn [15] and is illustrated in Fig. 3.2. In this figure, for inclusion size above r^* both branches are energetically equally favorable. The analytic expression for the associated critical length scale is given by Eq. 3.25.

$$r^* = \frac{3(1+\delta-2\nu_{incl})^2(1+\kappa\delta)\gamma}{4\mu_{incl}\delta(1-\delta)(1+\kappa)\epsilon^{*2}} \tag{3.25}$$

where $\kappa = 3 - 4\nu$,$\delta = \mu_{incl}/\mu_{mat}$ and μ and ν are shear modulus and Poisson's ratio, respectively, in the designated phase. Here we consider a 2-D plane strain system, with Young's moduli of $E_{incl} = 100GPa$, $E_{mat} = 150GPa$, with Poisson's ratio of 1/3 for both

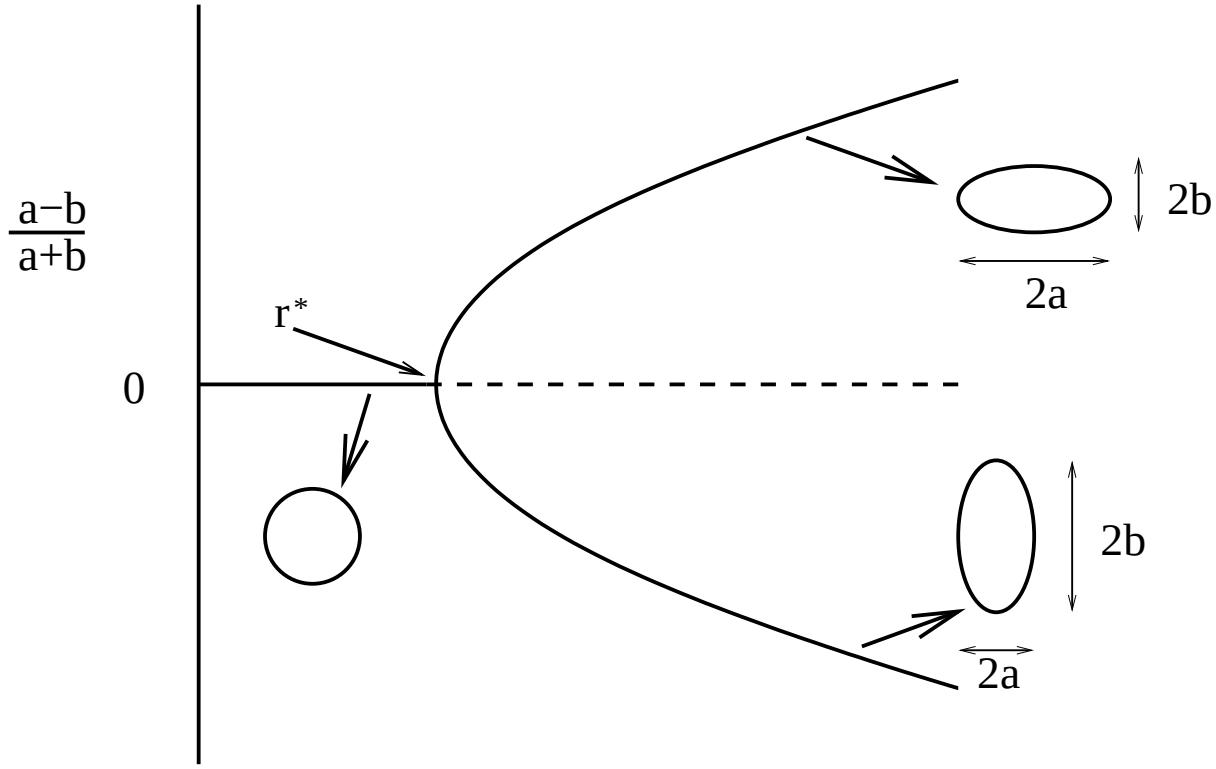

Figure 3.2: Schematic of shape transition

phases, dilatational transformational strain of 0.01 for inclusion, and the interface energy $\gamma = 50mJ/m^2$. For this particular system, critical size can be computed, Eq.3.25, to be $r^* = 35.62nm$. Since this system has four fold symmetry, we model only a quadrant, with a typical initial mesh shown in Figure. 3.3. As the equilibrium shape is dependent only on the volume and is independent of initial inclusion shape. To demonstrate this, we chose triangular (in one quadrant) inclusion shape as the intitial shape which is 'far' from the expected optimal inclusion shape. Further to model infinite extent of matrix large enough computational domain is chosen so that there is no significant interaction of interface fields with the boundary. The mesh chosen for these computations consists of linear triangular elements. Also, the initial mesh is such that elements adjacent to the interface have one of the edges aligned along the interface. To model symmetry, bottom face has been prescribed with zero vertical displacement, $u_2 = 0$, and left face has been prescribed with zero horizontal displacement, $u_1 = 0$. To maintain geometry of the computational domain during optimization, boundary conditions have been prescribed for undeformed coordinates (nodal coordinates) of the boundary nodes. In particular, nodes on faces with normals

along X_1 direction are allowed to move only in X_2 direction, i.e, prescribed X_1 component of undeformed coordinate, and vice versa.

Shape optimization has been accomplished with modified conjugate gradient solver described in the previous chapter. In this scheme, undeformed coordinate update is performed with configurational forces corresponding to equilibrium solution. Doing so would guarantee positive jacobian of the element.

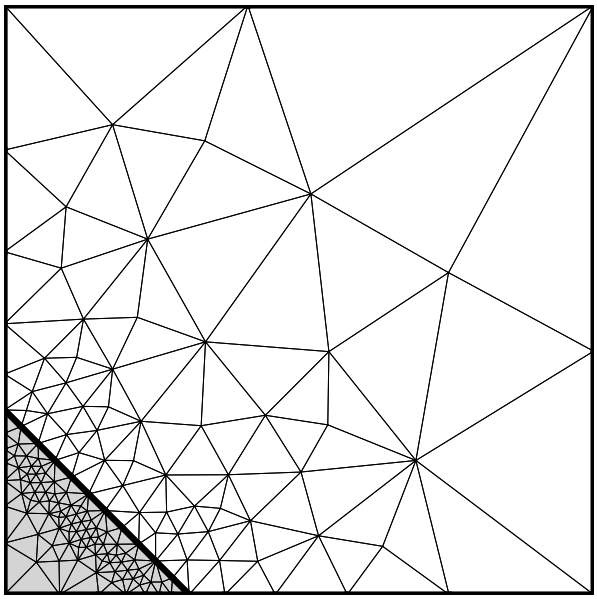

Figure 3.3: Typical initial mesh used for the calculations

Fig. 3.4 contains the result of the shape optimization and verifies the ability of the method to model symmetry bifurcation phenomena associated with the system. For a system with inclusion size $r = 31.91\text{nm}(< r^*)$, we obtain circular shape for the equilibrium shape, Fig. 3.4(b). In contrast, for the inclusion of size $r = 39.89\text{nm}(> r^*)$, equilibrium shape is elliptic, Fig. 3.4(d). This is in agreement with analytical predictions, Fig. 3.2. Further, in both cases we superimposed expected shapes on the optimal shapes for the purpose of comparison.

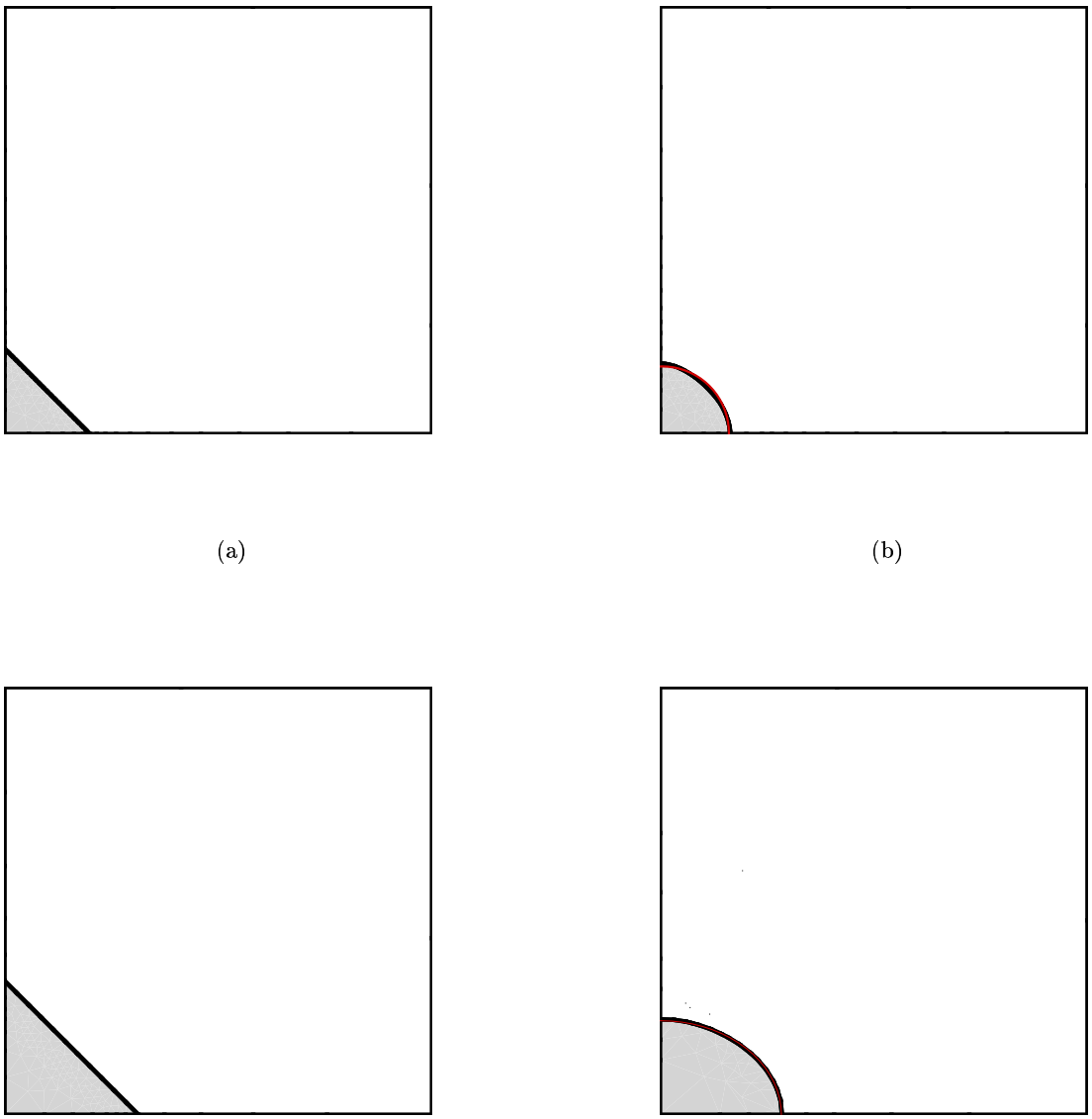

(a) (b)

(c) (d)

Figure 3.4: Shape transition of an isotropic system with dilatational misfit with transformational strain of precipitate :$\epsilon_x = \epsilon_y = 0.01$: a) Initial shape of particle with size 31.91 nm; b) Optimal shape of particle with size 31.91 nm; c) Initial shape of particle with size 39.89 nm; d) Optimal shape of particle with size 39.89 nm;.

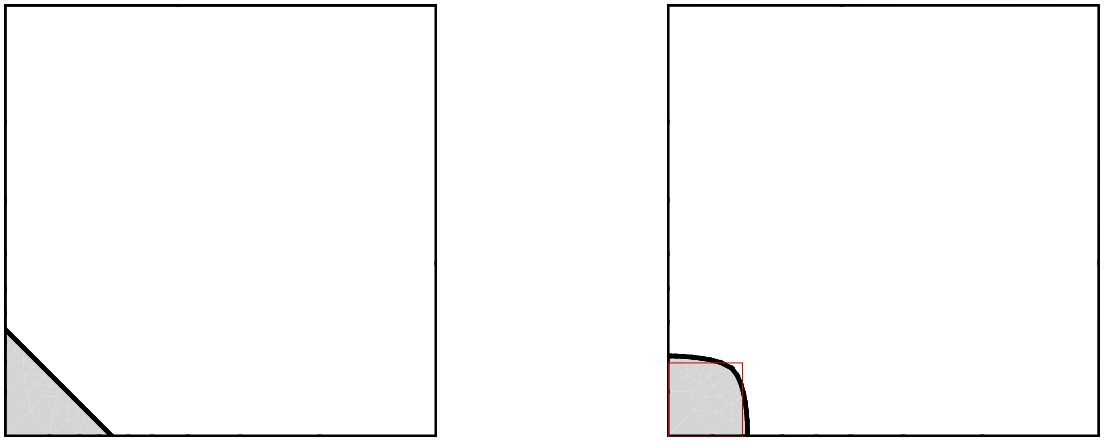

(a) (b)

Figure 3.5: optimal shape of orthotropic system with dilatational misfit with transformational strain of precipitate :$\epsilon_x = \epsilon_y = 0.01$: a) initial shape of particle with size 40.0nm; b) optimal shape of particle with size 40.0nm with superposed expected shape;

3.3.2 Orthotropic-dilatation misfit case

In this section we study the similar system as in the previous numerical example, except that in the present case material is linear elastic orthotropic material instead of linear isotrpic material, as was the case previously.

For the orthotropic case that we consider, we assume $C_{11} = C_{22} = 200$ GPa, $C_{12} = 100$ GPa and $C_{44} = 150$ GPa for both precipitate and matrix phases. Fig. 3.5 shows optimal shape of particle size of 40 nm, with dilatation misfit strain $\epsilon^* = 0.01$ which is of rectanglar shape. For this case analytical solutions for critical sizes are not available. However, qualitatively it compares well with the optimal shape obtained by Jog et al. [18] Thomson et al. [16] and by Schmidt and Gross [17] using different methods.

3.4 Summary and conclusions

In this chapter we demonstrated application of VALE method for shape optimization. As can be readily seen the variational formulation developed here is general enough to include finite deformation (in fact the derivation was for finite deformation) even though we

demonstrated it with linear elastic applications due to the lack of bench mark problems and analytic solutions. This method can also be used for structural optimization, wherein the boundary nodal motion corresponds to relevant objective function. Further, this method can be extended, based on gradient flow theory [33], to model diffusion induced shape transition, coarsening as in the case of Ostwald ripening.

Chapter 4

Variational integrators with horizontal variations

4.1 Introduction

In this chapter we develop a general framework for the variational integrators which account for horizontal variations, in particular nodal coordinate components. The resulting variational integrators are known to be symplectic and momentum conserving [28] and have remarkably good energy behavior. The main idea here is to develop algorithm for the update of undeformed (nodal) coordinates and deformed coordinates.

The discrete variational mechanics used in this chapter is based on space-time discretization of stationary action sum of Lagrangian mechanics. We render the discrete action sum so obtained stationary with respect to deformed and undeformed coordinates. The resulting equations correspond to linear momentum and material momentum (pseudo-momentum [14]) balance, respectively. The solution of discrete Euler-Lagrange equations corresponding to stationarity at every discrete time provides update for deformed and undeformed coordinates at discrete time intervals corresponding to temporal discretization. This update for undeformed coordinates provides mesh adaption scheme which is devoid of error estimates and mesh-to-mesh transfer. Further, the undeformed coordinate solution is guaranteed to satisfy linear momentum balance. Also in dynamic fracture, configurational (material) force component along tangential direction of the crack face of the crack nodes provide point-wise dynamic J-integral.

4.2 Variational formulation

We consider a solid occupying a region $B_0 \in \mathbb{R}^3$ in its reference undeformed configuration. The solid subsequently deforms under the action of externally applied forces and prescribed displacements. The deformation mapping $\boldsymbol{\varphi} : B_0 \to \mathbb{R}^3$ maps material points $\boldsymbol{X}$ in the reference configuration into their corresponding positions $\boldsymbol{x}$ in the deformed configuration $B = \boldsymbol{\varphi}(B_0)$, Fig. 4.1. The motion of the body is described by the deformation mapping

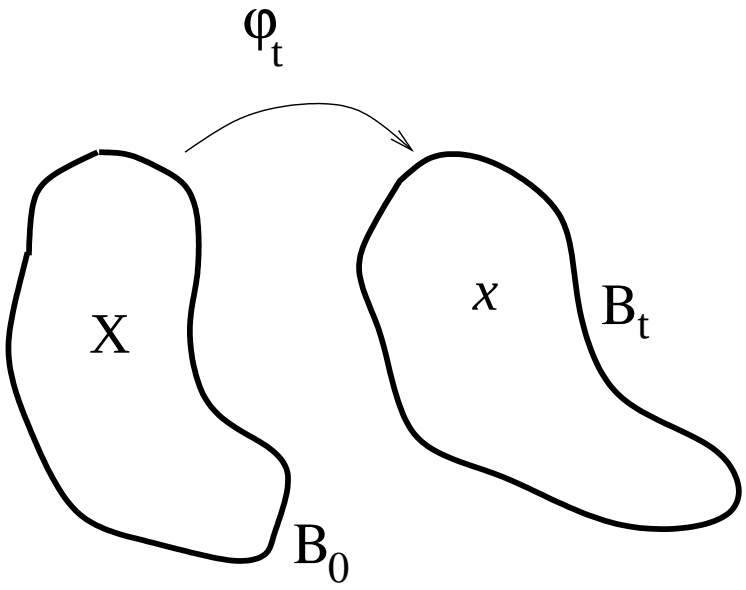

Figure 4.1: Deformation map

$$\boldsymbol{x} = \boldsymbol{\varphi}(\boldsymbol{X}, t), \boldsymbol{X} \in B_0 \tag{4.1}$$

which gives corresponding deformed configuration $B_t = \varphi_t(B_0)$. Thus, $\boldsymbol{x}$ is the location of material particle $\boldsymbol{X}$ at time t. The material velocity and acceleration field follow from Eq.4.1, $\dot{\boldsymbol{\varphi}}(\boldsymbol{X}, t)$ and $\ddot{\boldsymbol{\varphi}}(\boldsymbol{X}, t)$, $\boldsymbol{X} \in B_0$, respectively. The deformation gradient field follows as $\boldsymbol{F} = \nabla_0 \boldsymbol{\varphi}$, where ∇_0 is the material gradient. The deformation mapping is prescribed to take a prescribed value $\bar{\boldsymbol{\varphi}}$ over the displacement part ∂B_{01} of the undeformed boundary. This furnishes the Dirichlet boundary condition:

$$\varphi_i = \bar{\varphi}_i, \quad \text{on } \partial B_{01} \tag{4.2}$$

and

$$P_{iJ}N_J = \bar{T}_i, \quad \text{on } \partial B_{02} \tag{4.3}$$

Here $\boldsymbol{P}$ denotes the first Piola-Kirchhoff stress tensor, $\boldsymbol{N}$ is the unit normal to the undeformed boundary, and $\bar{\boldsymbol{T}}$ is the applied traction over the traction boundary $\partial B_{02} = \partial B_0 - \partial B_{01}$. For simplicity, we shall assume that the material is elastic, with strain-energy density $W(\boldsymbol{F})$. Under these assumptions, the constitutive relations take the form:

$$P_{iJ} = \frac{\partial W}{\partial F_{iJ}}(\boldsymbol{F}) \equiv P_{iJ}(\boldsymbol{F}) \tag{4.4}$$

The potential energy for the solid as a function of a deformation mapping $\boldsymbol{\varphi}(\boldsymbol{X}, t)$ satisfying essential boundary conditions (4.2) is given by

$$I[\boldsymbol{\varphi}, t] = \int_{B_0} W(\nabla_0 \boldsymbol{\varphi}) dV_0 - \int_{B_0} \rho_0 \boldsymbol{B} \cdot \boldsymbol{\varphi} dV_0 - \int_{\partial B_{02}} \bar{\boldsymbol{T}} \cdot \boldsymbol{\varphi} dS_0 \tag{4.5}$$

where $\boldsymbol{B}$ is the body force density per unit mass. The kinetic energy as a function of (material) velocity field $\dot{\varphi}(\boldsymbol{X}, t)$ is given by

$$K[\dot{\boldsymbol{\varphi}}] = \int_{B_0} \frac{\rho_0}{2} |\dot{\boldsymbol{\varphi}}|^2 dV_0 \tag{4.6}$$

where ρ_0 is the mass density. The functional form of Lagrangian is then

$$L[\boldsymbol{\varphi}, \dot{\boldsymbol{\varphi}}, t] = K[\dot{\boldsymbol{\varphi}}] - I[\boldsymbol{\varphi}, t] \tag{4.7}$$

Consider now a motion of the body during the time interval $[t_0, t_f]$. The action functional is given by

$$S[\boldsymbol{\varphi}] = \int_{t_0}^{t_f} L[\boldsymbol{\varphi}, \dot{\boldsymbol{\varphi}}, t] dt \equiv \int_{t_0}^{t_f} K[\dot{\boldsymbol{\varphi}}] - I[\boldsymbol{\varphi}, t] dt \tag{4.8}$$

As can be seen here the action function contains a space-time integral.

Hamilton's principle seeks the motions $\boldsymbol{\varphi}(\boldsymbol{X}, t)$ for which the action functional S is stationary with fixed initial and final deformed configurations B_{t_0} and B_{t_f}, satisfying the boundary conditions (4.2, 4.3). Let $D_i L$ be the partial derivative of L with its i^{th} argument,

then taking first variation with respect to $\boldsymbol{\varphi}$ will give Euler-Lagrange equations

$$D_1 L(\boldsymbol{\varphi}, \dot{\boldsymbol{\varphi}}, t) - \frac{d}{dt} D_2 L(\boldsymbol{\varphi}, \dot{\boldsymbol{\varphi}}, t) = 0 \tag{4.9}$$

for all $t \in [t_0, t_f]$, which gives the local linear momentum balance

$$\rho_0 \ddot{\boldsymbol{\varphi}} - \nabla_0 \cdot \boldsymbol{P} = \rho_0 \boldsymbol{B} \tag{4.10}$$

for $\boldsymbol{X} \in B_0$ and for all $t \in [t_0, t_f]$ and the traction boundary conditions on the Neumann boundary

$$\boldsymbol{P} \cdot \boldsymbol{N} = \boldsymbol{T} \tag{4.11}$$

on ∂B_2 and for all $t \in [t_0, t_f]$.

4.3 Discrete variational formulation

As mentioned earlier action functional (S) contains integral over both space (over B_0) and time (in the interval $[t_0, t_f]$). Introducing space-time discretization for finite element interpolation of the form:

$$\boldsymbol{\varphi}_h(\boldsymbol{X}) = \sum_{a=1}^{N} \boldsymbol{x}_a N_a(\boldsymbol{X}, t) = \sum_{e=1}^{m \times E} \sum_{a=1}^{n} \boldsymbol{x}_a^e N_a^e(\boldsymbol{X}, t) \tag{4.12}$$

where E is the number of elements in each time slab and m is the number of time slabs. Schematic of such a mesh for 1-D case is shown in the Fig. 4.2. In this schematic we have 2-D mesh wherein time is the other coordinate. In general, for n-(spatial) dimensional problem the resulting mesh is of n+1 dimension. Then the resulting discrete action sum (S_d) can be written as

$$\boldsymbol{S_d} = \sum_{i=1}^{m} \sum_{e=1}^{E} \int_{\Omega_e^i} \left[\frac{1}{2} \rho_0 \left(\sum_{a=1}^{n} x_{ja} N_{a,t} \right)^2 - W \left(\sum_{a=1}^{N} x_{ja} N_{a,J} \right) + \rho_0 B_j x_{ja} N_a \right] d\Omega_e^i \tag{4.13}$$

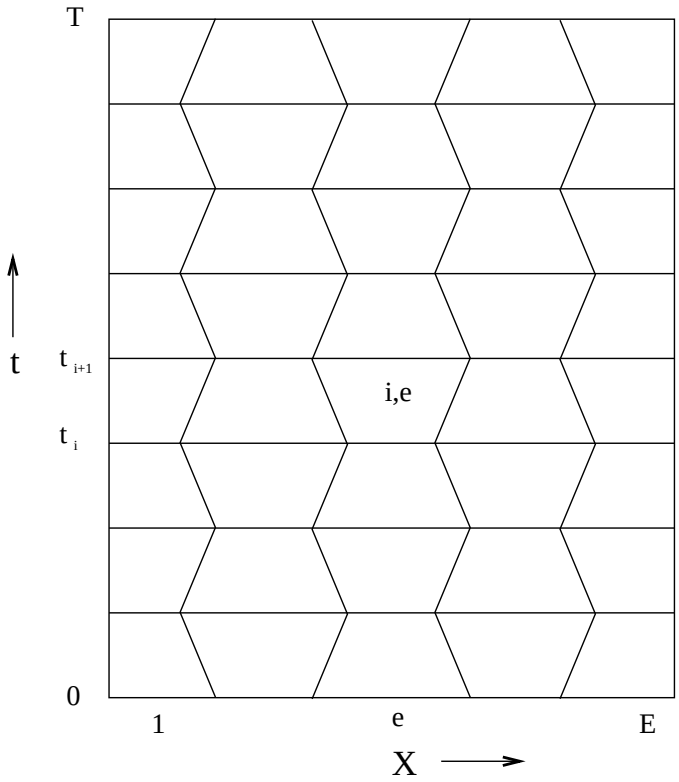

Figure 4.2: Schematic of space-time mesh where horizontal axis represents spatial reference domain

where Ω_e^i is the space-time domain of element e in time slab $[t_i, t_{i+1}]$. Invoking Hamilton's stationarity principle with vertical and horizontal variations

$$\sum_{i=2}^{m} \langle DS_d, \delta \boldsymbol{x}_i \rangle \delta \boldsymbol{x}_i + \langle DS_d, \delta \boldsymbol{X}_i \rangle \delta \boldsymbol{X}_i = 0 \tag{4.14}$$

where $\boldsymbol{x}_i$ and $\boldsymbol{X}_i$ are discrete deformed and undeformed (nodal) coordinates at time t_i. In the above we did not consider the time component of the horizontal variations. Further since variations in $\boldsymbol{x}_i$ and $\boldsymbol{X}_i$ are independent, the above equation can be written as a system of equations at each time step,

$$\begin{aligned} \boldsymbol{r} &= \langle DS_d, \delta \boldsymbol{x}_i \rangle = \tfrac{\partial S_d}{\partial \boldsymbol{x}_i} = 0 \\ \boldsymbol{R} &= \langle DS_d, \delta \boldsymbol{X}_i \rangle = \tfrac{\partial S_d}{\partial \boldsymbol{X}_i} = 0 \end{aligned} \quad i = 2 \ldots m \tag{4.15}$$

which enforce equilibrium of nodal forces and configurational (material) nodal forces, respectively. Further, for first order time interpolation, above system of equations at time

t_i contains contribution from $\boldsymbol{x}_{i-1}$,$\boldsymbol{X}_{i-1}$,$\boldsymbol{x}_i$,$\boldsymbol{X}_i$,$\boldsymbol{x}_{i+1}$ and $\boldsymbol{X}_{i+1}$. So, provided $\boldsymbol{x}_{i-1}$,$\boldsymbol{X}_{i-1}$,$\boldsymbol{x}_i$ and $\boldsymbol{X}_i$ are known, these equations provide update for $\boldsymbol{x}_{i+1}$ and $\boldsymbol{X}_{i+1}$.

Here, as can be seen from Eq. 4.15, configurational nodal force equilibrium is as fundamental as nodal force equilibrium. Further, configurational force equilibrium furnishes precise criterion for mesh optimality. System of configurational nodal force equilibrium together with system of nodal force equilibrium provide a coupled system of equations for the simultaneous solution of deformed ($\boldsymbol{x}_{i+1}$) and undeformed ($\boldsymbol{X}_{i+1}$) coordinates.

4.3.1 Element shape functions

Computation of element matrices requires shape functions of space-time element. To this end, shape functions are constructed as a product of spatial and temporal shape functions. Let ξ_1, ξ_2, ξ_3 be standard spatial coordinates and ξ_4 standard temporal coordinate with

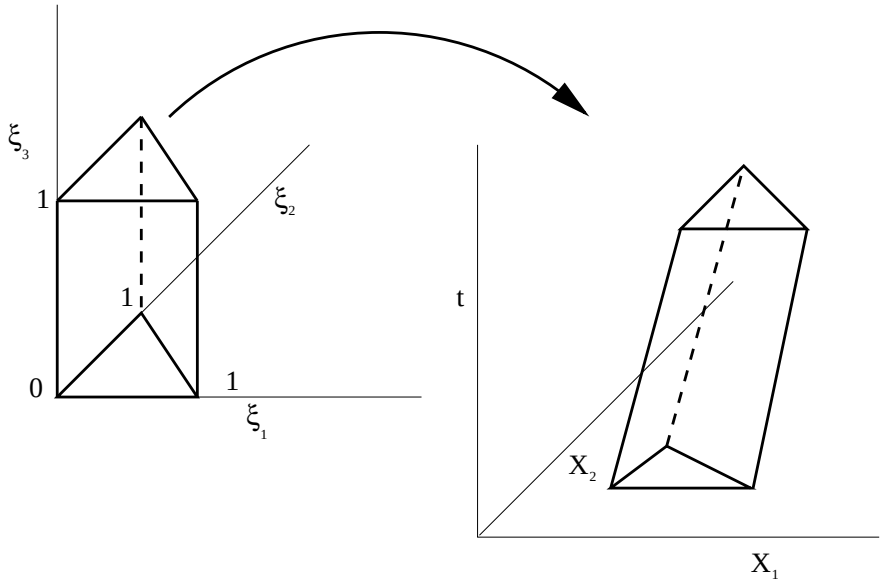

Figure 4.3: Schematic of a spacetime-element for 2-D spatial calculations

values between 0.0 and 1.0. Then the shape functions are given to be

$$N(\xi_1, \xi_2, \xi_3, \xi_4) = N^s(\xi_1, \xi_2, \xi_3) N^t(\xi_4) \tag{4.16}$$

where $N^s(\xi_1, \xi_2, \xi_3)$ and $N^t(\xi_4)$ are shape functions in space and time, respectively. This procedure allows independent interpolation in space and time. As mentioned earlier, it is preferable to have linear interpolation in time for the straight forward variational update.

Here we demonstrate the construction of shape function for a linear 3-D tetrahedral element and are given by

$$\begin{aligned}
N_1(\xi_1,\xi_2,\xi_3,\xi_4) &= (1-\xi_1-\xi_2-\xi_3)(1-\xi_4) \\
N_2(\xi_1,\xi_2,\xi_3,\xi_4) &= \xi_1(1-\xi_4) \\
N_3(\xi_1,\xi_2,\xi_3,\xi_4) &= \xi_2(1-\xi_4) \\
N_4(\xi_1,\xi_2,\xi_3,\xi_4) &= \xi_3(1-\xi_4) \\
N_5(\xi_1,\xi_2,\xi_3,\xi_4) &= (1-\xi_1-\xi_2-\xi_3)\xi_4 \\
N_6(\xi_1,\xi_2,\xi_3,\xi_4) &= \xi_1\xi_4 \\
N_7(\xi_1,\xi_2,\xi_3,\xi_4) &= \xi_2\xi_4 \\
N_8(\xi_1,\xi_2,\xi_3,\xi_4) &= \xi_3\xi_4
\end{aligned} \tag{4.17}$$

where N_1,N_2,N_3 and N_4 are shape functions corresponding to nodes at time t_i and N_5,N_6,N_7 and N_8 are shape functions corresponding to nodes at time t_{i+1}. Following, standard finite element procedure for finding shape function derivatives in space and time we begin writing shape function derivatives with respect to standard coordinates

$$\frac{\partial N_a}{\partial \xi_\alpha} = \frac{\partial X_i}{\partial \xi_\alpha}\frac{\partial N_a}{\partial X_i} \tag{4.18}$$

in which $\frac{\partial N_a}{\partial X_i}$ is a $(d+1)\times(d+1)$ matrix, where d is the spatial dimension of the problem. By inverting the above relationship, we obtain shape function derivatives in space and time

$$\frac{\partial N_a}{\partial X_i} = \left(\frac{\partial X_i}{\partial \xi_\alpha}\right)^{-1}\frac{\partial N_a}{\partial \xi_\alpha} \tag{4.19}$$

where X_{d+1} is time. Numerical quadrature for element matrices is constructed in similar manner as shape functions, by taking product of quadrature points in space ξ_1,ξ_2,ξ_3 and in time ξ_4.

4.3.1.1 Derivation of nodal and configurational nodal forces

In order to further explicate the stationarity conditions we begin by deriving nodal forces and configurational forces for an element i, e, Fig. 4.2, from $S_d^{i,e}$

$$\begin{aligned} r_{ck}^{i,e} &= \frac{\partial S_d^{i,e}}{\partial x_{ck}} \\ &= \int_{\Omega_e^i} (\rho_0 x_{c,t} N_{k,t} - P_{cJ} N_{k,J} + \rho_0 B_c N_k) d\Omega_e^i \qquad (4.20) \\ R_{Ck}^{i,e} &= \frac{\partial S_d^{i,e}}{\partial X_{Ck}} \\ &= \int_{\Omega_e^i} \frac{1}{2}\rho_0 x_{i,t} x_{i,t} N_{k,C} - \rho_0 x_{i,t} F_{iC} N_{k,t} \\ &\quad -(W\delta_{CJ} - P_{iJ}F_{iC} - \rho_0 B_j x_{ja} N_a) N_{k,J} d\Omega_e^i \qquad (4.21) \end{aligned}$$

and the corresponding Hessian is

$$\begin{aligned} \frac{\partial r_{ck}^{i,e}}{\partial x_{dl}} &= \int_{\Omega_e^i} (\rho_0 \delta_{cd} N_{l,t} N_{k,t} - C_{cJdF} N_{l,F} N_{k,J}) d\Omega_e^i \\ \frac{\partial r_{ck}^{i,e}}{\partial X_{Dl}} &= \int_{\Omega_e^i} \rho_0 x_{c,t} N_{k,t} N_{l,D} - \rho_0 F_{cD} N_{l,t} N_{k,t} - \rho_0 x_{c,t} N_{k,D} N_{l,t} - P_{cJ} N_{k,J} N_{l,t} \\ &\quad + P_{cJ} N_{k,D} N_{l,J} + C_{cJmN} F_{mD} N_{l,N} d\Omega_e^i \\ \frac{\partial R_{Ck}^{i,e}}{\partial x_{dl}} &= \int_{\Omega_e^i} \rho_0 x_{d,t} N_{l,t} N_{k,C} - \rho_0 F_{dC} N_{l,t} N_{k,t} - \rho_0 x_{d,t} N_{l,C} N_{k,t} \\ &\quad - P_{dJ} N_{l,J} N_{k,C} + P_{dJ} N_{k,J} N_{l,C} + C_{iJdN} F_{iC} N_{l,N} N_{k,J} d\Omega_e^i \\ \frac{\partial R_{Ck}^{i,e}}{X_{Dl}} &= \int_{\Omega_e^i} -\rho_0 x_{i,t} F_{iD} N_{l,t} N_{k,C} - \frac{1}{2}\rho_0 x_{i,t} x_{i,t} N_{k,D} N_{l,C} + \rho_0 F_{iD} F_{iC} N_{l,t} N_{k,t} \\ &\quad + \rho_0 x_{i,t} F_{iD} N_{l,C} N_{k,t} + \rho_0 x_{i,t} F_{iC} N_{k,D} N_{l,t} + \\ &\quad (W\delta_{CJ} - P_{iJ}F_{iC}) N_{k,D} N_{l,J} + (W\delta_{DM} - P_{iM}F_{iD}) N_{l,M} N_{k,C} \\ &\quad - C_{iJmN} F_{mD} F_{iC} N_{l,N} N_{k,J} - P_{iJ} F_{iD} N_{l,C} N_{k,J} \\ &\quad + (\frac{1}{2}\rho_0 x_{i,t} x_{i,t} N_{k,C} - \rho_0 x_{i,t} F_{iC} N_{k,t}) N_{l,D} + P_{iJ} F_{iC} N_{k,J} N_{l,D} d\Omega_e^i \qquad (4.22) \end{aligned}$$

The corresponding equations for linear-elastic case are

$$\begin{aligned} r^{i,e}_{ck} &= \frac{\partial S^{i,e}_d}{\partial u_{ck}} \\ &= \int_{\Omega^i_e} (\rho_0 u_{c,t} N_{k,t} - \sigma_{cj} N_{k,j} + \rho_0 B_c N_k) d\Omega^i_e \qquad (4.23) \\ R^{i,e}_{ck} &= \frac{\partial S^{i,e}_d}{\partial X_{ck}} \\ &= \int_{\Omega^i_e} \frac{1}{2}\rho_0 u_{i,t} u_{i,t} N_{k,c} - \rho_0 u_{i,t} u_{i,c} N_{k,t} \\ &\quad -W N_{k,C} + \sigma_{ij} u_{i,c} N_{k,j} + \rho_0 B_j x_{ja} N_a N_{k,C} d\Omega^i_e \qquad (4.24) \end{aligned}$$

and the corresponding Hessian is

$$\begin{aligned} \frac{\partial r^{i,e}_{ck}}{\partial u_{dl}} &= \int_{\Omega^i_e} (\rho_0 \delta_{cd} N_{l,t} N_{k,t} - \frac{1}{2} * (C_{cjdn} N_{l,n} + C_{cjmd} N_{l,m}) N_{k,j}) d\Omega^i_e \\ \frac{\partial r^{i,e}_{ck}}{\partial X_{dl}} &= \int_{\Omega^i_e} \rho_0 u_{c,t} N_{k,t} N_{l,d} - \rho_0 u_{c,d} N_{l,t} N_{k,t} - \rho_0 u_{c,t} N_{k,d} N_{l,t} + \frac{1}{2} C_{cjmn} (u_{m,d} N_{l,n} + u_{n,d} N_{l,m}) N_{k,j} \\ &\quad + \sigma_{cj} N_{k,d} N_{l,j} - \sigma_{cj} N_{k,j} N_{l,d} d\Omega^i_e \\ \frac{\partial R^{i,e}_{ck}}{\partial u_{dl}} &= \int_{\Omega^i_e} \rho_0 u_{d,t} N_{l,t} N_{k,c} - \rho_0 u_{d,c} N_{l,t} N_{k,t} - \rho_0 u_{d,t} N_{l,c} N_{k,t} \\ &\quad - \sigma_{dj} N_{l,j} N_{k,c} + \sigma_{dj} N_{k,j} N_{l,c} + \frac{1}{2} u_{i,c} N_{k,j} (C_{ijdn} N_{l,m} + C_{ijmd} N_{l,m}) d\Omega^i_e \\ \frac{\partial R^{i,e}_{Ck}}{X_{dl}} &= \int_{\Omega^i_e} -\rho_0 u_{i,t} u_{i,d} N_{l,t} N_{k,c} - \frac{1}{2}\rho_0 u_{i,t} u_{i,t} N_{k,d} N_{l,c} + \rho_0 u_{i,d} u_{i,c} N_{l,t} N_{k,t} + \\ &\quad + \rho_0 u_{i,t} u_{i,d} N_{l,c} N_{k,t} + \rho_0 u_{i,t} u_{i,c} N_{k,d} N_{l,t} \\ &\quad + \sigma_{ij} u_{i,d} N_{l,j} N_{k,c} + W N_{k,d} N_{l,c} - \frac{1}{2} C_{ijmn} (u_{m,d} N_{l,n} + u_{n,d} N_{l,m}) u_i c N_{k,j} \\ &\quad - \sigma_{ij} u_{i,d} N_{l,c} N_{k,j} - \sigma_{ij} u_{i,c} N_{k,d} N_{l,j} + \\ &\quad (\frac{1}{2}\rho_0 u_{i,t} u_{i,t} N_{k,c} - \rho_0 u_{i,t} u_{i,c} N_{k,t} - W N_{k,c} + \sigma_{ij} u_{i,c} N_{k,j}) N_{l,d} d\Omega^i_e \qquad (4.25) \end{aligned}$$

which correspond to nodal force and configurational nodal force contributions from element i, e. It may be noted that element i, e contributes to nodal force equilibrium and configurational nodal force equilibrium equations at discrete times t_i and t_{i+1}. Assembling these elemental contributions results in the update equations for $\boldsymbol{x}_{i+1}$ and $\boldsymbol{X}_{i+1}$ at time t_{i+1}, which correspond to stationarity of discrete action sum S_d at time t_i.

4.3.2 Solution method

From the above discussion, updates for $\boldsymbol{x}_{i+1}$ and $\boldsymbol{X}_{i+1}$ require the solution of $\boldsymbol{r}_i = 0$ and $\boldsymbol{R}_i = 0$, which correspond to nodal and configurational nodal force equilibrium at time t_i. One obvious choice of solution is by Newton-Raphson method. However here Newton-Raphson method should be applied in two levels, one correspond to the undeformed coordinate update, which in turn contains Newton-Raphson solver for equilibrium solution. During the deformed coordinate solution, undeformed coordinates remain fixed, i.e., we obtain equilibrium solution over a fixed mesh. This approach guarantees that during undeformed coordinate update elements maintain positive jacobian, since nodal configurational forces used for this update correspond to nodal force equilibrium and hence are physical. This has similarities to that of the modified conjugate gradient solver in that it also has two levels and during coordinate update computations are done with deformed coordinates corresponding to the equilibrium solution.

4.4 Numerical tests

In this section we report results of numerical test which establish the accuracy and long-term energy behavior of the variational integrator. Here we conducted tests for 1-D linear elastic rod with elastic modulus $E = 2.0\ GPa$ and $\rho_0 = 1000 Kg/m^3$. In this numerical test we used 1-D linear elastic rod which is under uniform tension in the beginning, i.e., uniform strain initial condition, corresponding to initial free end displacement u_0 while the other end is fixed, as shown in Fig. 4.4. Corresponding initial conditions for deformed and undeformed coordinates are shown in Fig. 4.5. The mesh consists of 2-noded linear 1-D elements.

Figure 4.4: 1-D linear elastic string

As can be readily seen, this is a conservative system as there is neither forcing nor dissipation. So, we expect the total energy to be conserved. In addition, due to hyper-

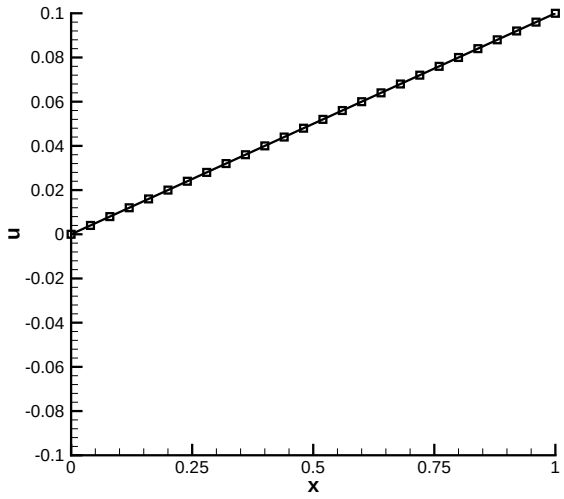

Figure 4.5: Initial conditions for 1d-string problem

bolic nature of the governing equation (4.10) we would expect discontinuities in gradients, which in turn demonstrates the methods ability to resolve moving gradients. This can be seen from the Fig. 4.6, in which nodal locations and the corresponding nodal displacements at various discrete times are shown. As can be readily observed, nodes try to converge onto location of discontinuity, which will enable it to resolve the regions of discontinuity. Further, we also plot in Fig. 4.7 variation of total energy with time. Since the system is conservative we expect the system to conserve total energy. As can be seen from Fig. 4.7 in which total energy has good longtime energy behavior. The small drift can be attributed to the fact during the simulation we did not resort to time-adaption, i.e., time-steps used in the simulation do not correspond to the stationarity condition corresponding to time component of horizontal variations. Also loss of total energy can be attributed to the introduction of the numerical viscosity by recourse to Discrete Lagrange-d'Alembert principle [13]. This has been necessiated because in two parts on either side of the discontinuity strain is constant. However for the constant strain any nodal distribution satisfies configurational equilibrium, i.e., nodal distribution is non-unique for constant strain. Introduction of the artificial viscosity regularizes and hence provides solution for nodal coordinates.

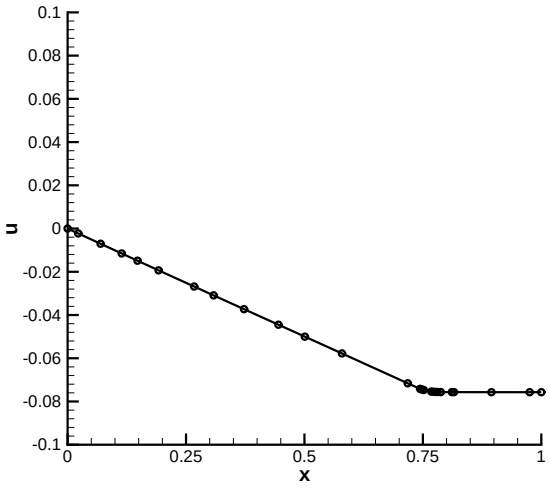

(a)

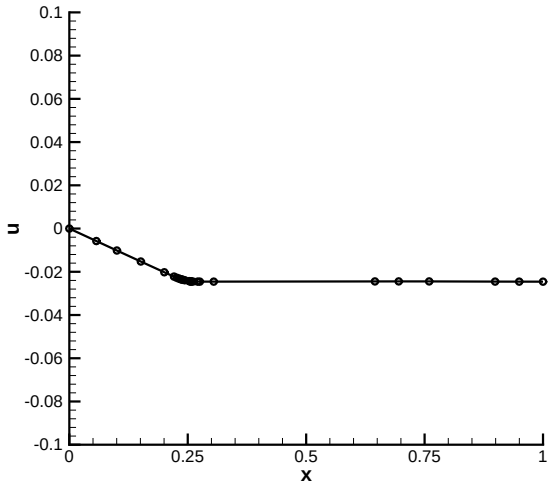

(b)

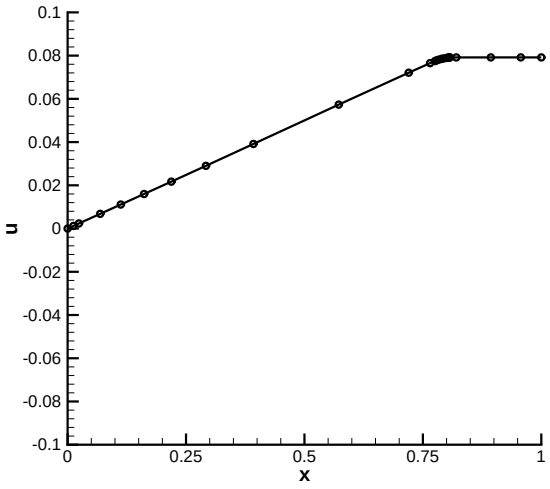

(c)

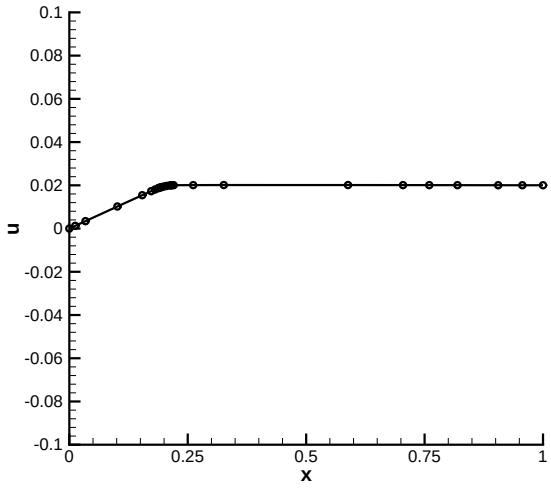

(d)

Figure 4.6: Nodal distributions at various times

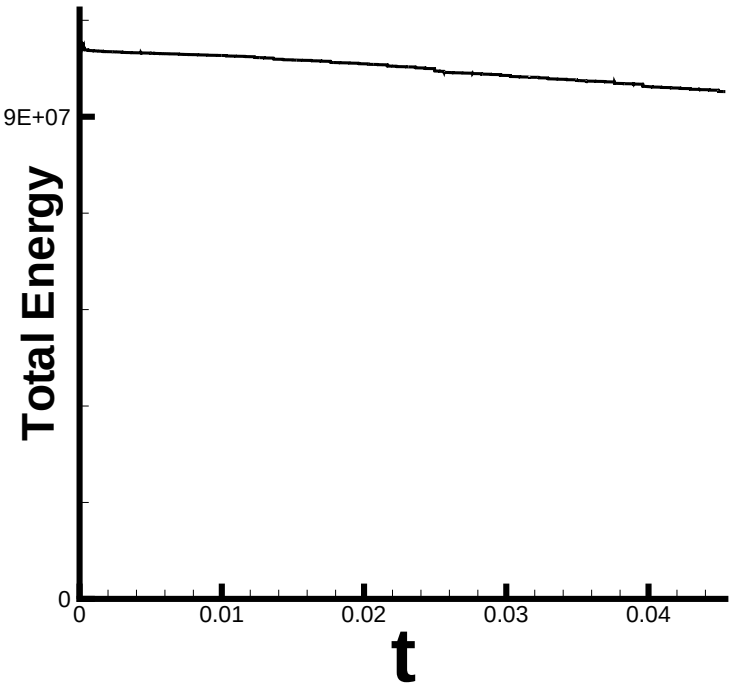

Figure 4.7: Total energy vs. time

4.5 Summary and conclusions

We have developed a novel variational integrator in which in addition to nodal variables, mesh itself is the solution. In addition, the resulting algorithm is symplectic-momentum preserving with good long-term energy behavior. The resulting mesh-adaption algorithm has the following advantages.

1. It is variationally consistent and based on sound principles. In addition, it provides precise criterion for optimal mesh, i.e., nodal configurational equilibrium (4.15). The optimal mesh so obtained provides the most accurate solution for a given number of nodes.

2. Does not involve error estimation.

3. Does not involve mesh-to-mesh transfer and hence devoid of associated interpolation errors. Further, it guarantees nodal force equilibrium.

4. In this scheme only nodal coordinates change and everything else corresponding to

mesh description remains same. This in turn obviates mesh remapping onto processors in parallel mesh adaption and hence is ideally suited for parallel computation.

5. In general each time slab need not be of fixed time step, i.e., $t_i - t_{i-1} \neq t_{i+1} - t_i$. Further, each node can evolve at it's own pace and hence this integrator is similar to AVI with the difference instead of elements in this case nodes can march at their own pace.

In this framework since both deformed and undeformed coordinates are solutions we can interpret, Eulerian (fixed deformed coordinates) and Lagrangian (fixed reference coordinates) can be considered as special cases of this formulation. This interpretation is particularly useful when considering variationally consistent Euler-Lagrange coupling, in which case it involves choosing appropriate boundary conditions on deformed and undeformed coordinates.

Chapter 5

Tetrahedral composite finite elements

5.1 Introduction

Camacho and Ortiz [41, 40] briefly described triangular and tetrahedral elements constructed by assembling linear subtriangles and tetrahedra and coupling them to a continuous linear strain field over the assemblage. They called these elements *composite* triangular and tetrahedral, or CT, elements. The advantages of these elements arise primarily in explicit time integration and contact-impact problems, where the lumped mass of their midside nodes is well-matched to their corner node masses. This feature effectively overcomes the difficulties inherent to quadratic simplicial elements, for which the row-sum method of lumping results in zero or negative corner masses. In fact the significant improvement in the simulation of ballistic impact problems has been reported by Knap [49] when performed with the present element over that that with ten-noded isoparametric element. Furthermore, the volumetric locking which characterizes linear simplicial elements is eliminated. Thus the composite elements appear to combine the best attributes of linear simplicial elements, including the ease of mesh generation, without their drawbacks.

Guo *et al.* [43] have presented a detailed analysis of several composite triangular elements and have established their basic behavior. This study has shown that the CT elements have a rate of convergence in energy norm comparable to the six-node element for compressible materials though the rate of convergence in the displacements is of the same order as the linear-displacement three-node triangle. The elements pass the patch test in arbitrarily distorted configurations. For incompressible problems, the performance

of the linear strain element is not as satisfactory. Guo *et al.* [43] proposed an alternative composite triangle in which the volumetric strain is assumed constant over the assemblage and showed that this element satisfies the Babuška-Brezzi criterion.

In this chapter we propose and analyze a composite tetrahedral element. The proposed ten-node CT element is a composite of twelve 4-node tetrahedral elements with linear displacement field in each one of them. The relation between displacements and deformations is enforced weakly by recourse to the Hu-Washizu principle (e. g., [46, 40, 41, 43]). The formulation of the element allows for fully nonlinear kinematics. We verify that the element passes the patch test in arbitrarily distorted configurations. In addition, for compressible materials the CT element is found to possess a convergence rate in the energy and pressure norms comparable to linear elements. Finally, we verify that the element passes the Babuška-Brezzi criterion and performs well in the near-incompressible limit.

5.2 Model problem

We consider a solid occupying a region $B_0 \in \mathbb{R}^3$ in its reference undeformed configuration. The solid subsequently deforms under the action of externally applied forces and prescribed displacements. The deformation mapping $\boldsymbol{\varphi} : B_0 \to \mathbb{R}^3$ maps material points $\boldsymbol{X}$ in the reference configuration into their corresponding positions $\boldsymbol{x}$ in the deformed configuration $B = \boldsymbol{\varphi}(B_0)$. The deformation gradient field follows as $\boldsymbol{F} = \nabla_0 \boldsymbol{\varphi}$, where ∇_0 is the material gradient. In components:

$$F_{iJ} = \frac{\partial \varphi_i}{\partial X_J}, \quad \text{in } B_0 \tag{5.1}$$

Here and subsequently, we use upper (respectively, lower) case indices to denote components of vector fields defined over the undeformed (respectively, deformed) configuration. The deformation mapping is prescribed to take a prescribed value $\bar{\boldsymbol{\varphi}}$ over the displacement part ∂B_{01} of the undeformed boundary. This furnishes the boundary condition:

$$\varphi_i = \bar{\varphi}_i, \quad \text{on } \partial B_{01} \tag{5.2}$$

Additionally, the solid is in equilibrium, which requires:

$$P_{iJ,J} + \rho_0 B_i = 0, \quad \text{in } B_0 \tag{5.3}$$

and

$$P_{iJ}N_J = \bar{T}_i, \quad \text{on } \partial B_{02} \tag{5.4}$$

Here $\boldsymbol{P}$ denotes the first Piola-Kirchhoff stress tensor, ρ_0 is the mass density per unit undeformed volume, $\boldsymbol{B}$ is the body force density per unit mass, $\boldsymbol{N}$ is the unit normal to the undeformed boundary, and $\bar{\boldsymbol{T}}$ is the applied traction over the traction boundary $\partial B_{02} = \partial B_0 - \partial B_{01}$. For simplicity, we shall assume that the material is elastic, with strain-energy density $W(\boldsymbol{F})$. Under these assumptions, the constitutive relations take the form:

$$P_{iJ} = \frac{\partial W}{\partial F_{iJ}}(\boldsymbol{F}) \equiv P_{iJ}(\boldsymbol{F}) \tag{5.5}$$

With a view to formulating finite-element approximations, we begin by re-stating the preceding equations in variational form. The conventional displacement finite-element method may be regarded as the result of effecting a constrained minimization of the potential energy:

$$\Phi = \int_{B_0} [W(\nabla_0 \boldsymbol{\varphi}) - \rho_0 B_i \varphi_i] dV_0 - \int_{\partial B_{02}} \bar{T}_i \varphi_i dS_0 \tag{5.6}$$

among all finite-element deformation mappings. More general finite-element methods may be derived from the Hu-Washizu principle. The Hu-Washizu potential of the solid is

$$\begin{aligned} I[\boldsymbol{\varphi}, \boldsymbol{F}, \boldsymbol{P}] &= \int_{B_0} [W(\boldsymbol{F}) + P_{iJ}(\varphi_{i,J} - F_{iJ}) - \rho_0 B_i \varphi_i] dV_0 \\ &- \int_{\partial B_{01}} P_{iJ} N_J (\varphi_i - \bar{\varphi}_i) dS_0 - \int_{\partial B_{02}} \bar{T}_i \varphi_i dS_0 \end{aligned} \tag{5.7}$$

The stationarity of I demands:

$$\int_{B_0} (P_{iJ} \delta\varphi_{i,J} - \rho_0 B_i \delta\varphi_i) dV_0 - \int_{\partial B_{01}} P_{iJ} N_J \delta\varphi_i dS_0 - \int_{\partial B_{02}} \bar{T}_i \delta\varphi_i dS_0 = 0 \tag{5.8}$$

$$\int_{B_0} [W_{,F_{iJ}}(\boldsymbol{F}) - P_{iJ}] \delta F_{iJ} dV_0 = 0 \tag{5.9}$$

$$\int_{B_0} (\varphi_{i,J} - F_{iJ}) \delta P_{iJ} dV_0 - \int_{\partial B_{01}} \delta P_{iJ} N_J (\varphi_i - \bar{\varphi}_i) dS_0 = 0 \tag{5.10}$$

which is a weak re-statement of the field equations and boundary conditions of the problem. The appeal of the Hu-Washizu principle in the present context is that it allows for the independent interpolation of displacements, deformations and stresses. The use of the Hu-Washizu principle to formulate mixed elements was pioneered by Simó [45].

5.3 Element description

The proposed element consists of twelve four-node sub-elements, each of which is equipped with linear displacement interpolation. This piecewise linear displacement interpolation scheme is coupled to linear assumed deformation and stress fields defined over the entire domain of the element. One motivation for this choice of interpolation is to obtain an element in which lumped nodal masses are unambiguously and appropriately defined and are well-matched to contact tractions in impact problems. This is accomplished by interpolating displacements in a piecewise linear fashion. The choice of deformation and stress interpolation is designed so as to introduce four volume constraints per element in the near-incompressible limit.

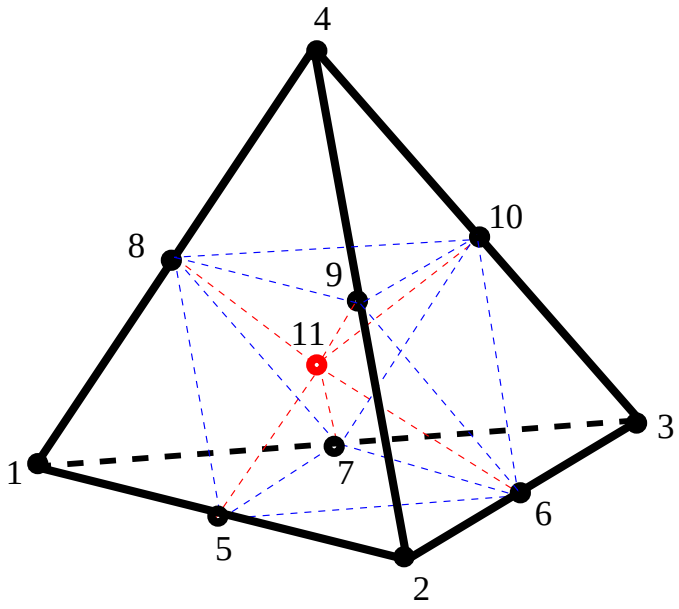

Figure 5.1: The geometry and nodal numbering convention of the CT3D composite element.

The geometry and nodal numbering convention of the element are depicted in Fig. 5.1. It should be carefully noted that the element edges need not be straight, i. e., the center node of the edges need not be at the midpoint of the segment defined by the corresponding vertices. We additionally introduce an auxiliary node at position:

$$\boldsymbol{X}_{11} = \frac{1}{6}\sum_{a=5}^{10} \boldsymbol{X}_a \tag{5.11}$$

Tetrahedron	node 1	node 2	node 3	node 4
1	1	5	7	8
2	2	6	5	9
3	3	7	6	10
4	4	9	8	10
5	5	9	6	11
6	6	9	10	11
7	10	9	8	11
8	8	9	5	11
9	5	6	7	11
10	6	10	7	11
11	10	8	7	11
12	8	5	7	11

Table 5.1: Connectivity array for the 12 sub-elements of the CT3D composite element.

where $\boldsymbol{X}_a, a = 1, \ldots 10$ are the undeformed nodal coordinates. Likewise, the position of the auxiliary node in the deformed configuration is constrained to be:

$$\boldsymbol{x}_{11} = \frac{1}{6} \sum_{a=5}^{10} \boldsymbol{x}_a \tag{5.12}$$

in accordance with the assumed linear interpolation. The introduction of an auxiliary eleventh node such as described ensures that, in its regular tetrahedral configuration, the element possesses all the expected symmetries. In particular, all the mid-edge nodes are given the same weight. The twelve sub-elements are defined by the connectivity array in Table 5.1.

The interpolation scheme just described defines a set of piecewise linear shape functions $\{N_a,\ a = 1, \ldots, 10\}$ defined over the undeformed domain of the element. In particular, the interpolated deformation mapping is

$$\boldsymbol{\varphi}(\boldsymbol{X}) = \sum_{a=1}^{10} \boldsymbol{x}_a \boldsymbol{N}_a(\boldsymbol{X}) \tag{5.13}$$

where $\{\boldsymbol{x}_a,\ a = 1, \ldots, 10\}$ are deformed nodal coordinates.

Independently of the displacement interpolation just described, we adopt an 'assumed'

linear representation of the deformation and stress fields of the form:

$$\bar{\boldsymbol{F}}(\boldsymbol{X}) = \sum_{a=1}^{4} \boldsymbol{F}_a \lambda_a(\boldsymbol{X}) \tag{5.14}$$

$$\bar{\boldsymbol{P}}(\boldsymbol{X}) = \sum_{a=1}^{4} \boldsymbol{P}_a \lambda_a(\boldsymbol{X}) \tag{5.15}$$

where $\{\lambda_a,\ a = 1, \ldots, 4\}$ are the barycentric coordinates associated with the four vertices of the parent element and $\{\boldsymbol{F}_a,\ a = 1, \ldots, 4\}$ and $\{\boldsymbol{P}_a,\ a = 1, \ldots, 4\}$ are matrices of coefficients. Evidently, the assumed deformations are not the gradients of the interpolated deformation mapping (5.13) in general. Likewise, the assumed stress field does not follow from an application of the constitutive relations to the gradients of the interpolated mapping. Instead, we enforce these relations weakly in the sense of eqs. (5.8), (5.9) and (5.10). In particular, from eq. (5.10) we obtain the system of equations:

$$\sum_{b=1}^{4} \left\{ \int_{\Omega_0} \lambda_a \lambda_b \, dV_0 \right\} F_{iJb} = \left\{ \sum_{b=1}^{10} \int_{\Omega_0} \lambda_a N_{b,J} \, dV_0 \right\} x_{ib} \tag{5.16}$$

where Ω_0 is the undeformed domain of the element and we have assumed that the displacement boundary conditions are identically satisfied by the displacement interpolation. Solving (5.16) for the coefficients $\boldsymbol{F}_a$ and inserting the result into (5.14) yields the relation

$$\bar{F}_{iJ}(\boldsymbol{X}) = \sum_{a=1}^{10} x_{ia} \bar{L}_{aJ}(\boldsymbol{X}) \tag{5.17}$$

where

$$\bar{L}_{aJ}(\boldsymbol{X}) = \sum_{b=1}^{4} \sum_{c=1}^{4} \lambda_c(\boldsymbol{X}) \, M^{-1}_{cb} \int_{\Omega_0} \lambda_b N_{a,J} \, dV_0 \tag{5.18}$$

and we write

$$M_{bc} = \int_{\Omega_0} \lambda_b \lambda_c \, dV_0 \tag{5.19}$$

Eq.(5.17) gives the assumed deformation field in terms of the deformed nodal coordinates and replaces the conventional relation

$$\boldsymbol{F}_{iJ}(\boldsymbol{X}) = \sum_{a=1}^{10} x_{ia} N_{a,J}(\boldsymbol{X}) \equiv \sum_{a=1}^{10} x_{ia} L_{aJ}(\boldsymbol{X}) \tag{5.20}$$

λ_1	λ_2	λ_3	λ_4	Quadrature weight
1/4	1/4	1/4	1/4	$(V_5 + V_7 + V_{10} + V_{12})/2 + V_6 + V_8 + V_9 + V_{11}$
1/2	1/6	1/6	1/6	$V_1 + V_{12}/2$
1/6	1/2	1/6	1/6	$V_2 + V_5/2$
1/6	1/6	1/2	1/6	$V_3 + V_{10}/2$
1/6	1/6	1/6	1/2	$V_4 + V_7/2$

Table 5.2: Five-point quadrature rule.

of the displacement finite-element method. We also note that the matrix inversion in (5.18) needs to be carried out only once in the course of a calculation.

Taking variations in (5.17) gives the relation

$$\delta \bar{F}_{iJ}(\boldsymbol{X}) = \sum_{a=1}^{10} \delta x_{ia} \bar{L}_{aJ}(\boldsymbol{X}) \tag{5.21}$$

which upon substitution into (5.8) yields the internal and external force arrays:

$$f_{ia}^{\text{int}} = \int_{\Omega_0} \bar{P}_{iJ} \bar{L}_{aJ} \, dV_0 \tag{5.22}$$

$$f_{ia}^{\text{ext}} = \int_{\Omega_0} \rho_0 B_i N_a \, dV_0 + \int_{\partial\Omega_{02}} \bar{T}_i N_a \, dS_0 \tag{5.23}$$

In arriving at these expressions we have restricted $\delta\boldsymbol{\varphi}$ to satisfy homogeneous essential boundary conditions, i. e., we have required that $\delta\varphi_i = 0$ on ∂B_{01}. We also note that in (5.23) $\partial\Omega_{02}$ denotes $\partial\Omega_0 \cap \partial B_{02}$, i. e., it is the part of the boundary of the element, possibly empty, which lies on the traction boundary.

Finally, we turn to the weak form (5.9) of the constitutive relations. Inserting (5.14) and (5.15) into (5.9) and solving the resulting system of linear equations gives:

$$P_{iJb} = \sum_{a=1}^{4} M_{ba}^{-1} \int_{B_0} P_{iJ}(\bar{\boldsymbol{F}}) \, \lambda_a dV_0 \tag{5.24}$$

and the stress field follows in the form:

$$\bar{P}_{iJ} = \sum_{a=1}^{4} \sum_{b=1}^{4} \lambda_b(\boldsymbol{X}) \, M_{ba}^{-1} \int_{B_0} P_{iJ}(\bar{\boldsymbol{F}}) \, \lambda_a dV_0 \tag{5.25}$$

This field may now be used in (5.22) to compute the internal force array.

In calculations, we evaluate the integrals in (5.19) and (5.22) by the five-point Gaussian quadrature rule (as when compared to four-points quadrature scheme required for the usual isoparametric element) defined in Table 5.2. In this table V_i denotes the volume of sub-element i. In principle, the integral in the stress-reduction formula (5.25) could be computed by the same means. However, this would render the computation of the stresses somewhat costly. Instead, we choose to satisfy the constitutive relations strongly by simply evaluating (5.5) pointwise using the assumed deformation field (5.17). The resulting internal forces are

$$f_{ia}^{\text{int}} = \int_{\Omega_0} P_{iJ}(\bar{\boldsymbol{F}}) \bar{L}_{aJ} \, dV_0 \tag{5.26}$$

This expression may be obtained directly by rendering stationary the 'assumed' potential energy:

$$\Phi = \int_{B_0} [W(\bar{\boldsymbol{F}}) - \rho_0 B_i \varphi_i] \, dV_0 - \int_{\partial B_{02}} \bar{T}_i \varphi_i \, dS_0 \tag{5.27}$$

Note that, in this expression, the strain energy is evaluated from the assumed deformation field directly. This implementation is in the spirit of Hughes's $\bar{\boldsymbol{B}}$ method for anisotropic linear elasticity [44], in which the discrete strain operator, or $\boldsymbol{B}$ matrix, is replaced by an assumed matrix $\bar{\boldsymbol{B}}$ in the strain energy density. The resulting finite-element method may be obtained from the standard displacement finite-element method by formally replacing the material shape-function gradients $N_{a,J}$ by the the array $\bar{L}_{aJ}$ defined in (5.18). This substitution may conveniently be made at the shape-function routine level, and the remaining structure of the element routine is identical to that of the displacement finite-element method.

We also note that a lumped-mass matrix for the composite element may simply be computed by assembling the standard lumped-mass matrices of the twelve four-node sub-elements. The resulting nodal mass distribution is depicted in Fig. 5.2. As is evident from this figure, all nodal masses are strictly positive. This is in contrast to the lumped-masses for the quadratic ten-node element obtained by the row-sum method, which are negative at the corner nodes.

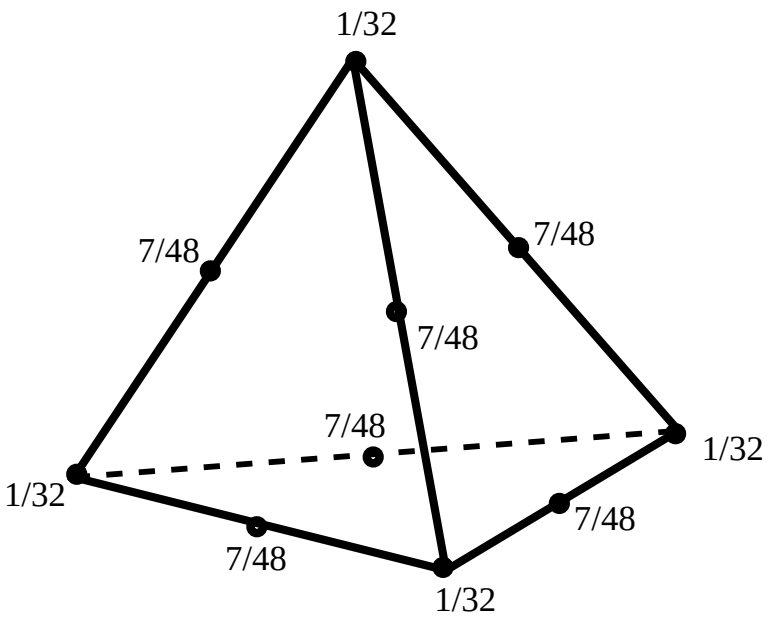

Figure 5.2: Lumped-mass distribution for the CT3D composite element.

5.4 Numerical tests

In this section we report the results of a number of standard tests which establish the accuracy, stability and convergence characteristics of the CT3D composite element. As a first elementary test, we have verified that the element passes the patch test in arbitrary distorted configurations, and that the tangent stiffness matrices are not rank-deficient and, therefore, are devoid of spurious zero-energy modes. It should be noted that, for the patch test to be satisfied for arbitrary element geometries, care must be exercised to employ the same quadrature scheme in the calculations of the assumed shape-function gradients and the element force and stiffness arrays. We have also assessed the convergence characteristics of the element in selected linear benchmark cases, and demonstrated the stability of the element in the near-incompressible limit with the aid of the inf-sup test of Babuška and Brezzi [37, 39]. These tests are subsequently discussed in turn.

5.4.1 Convergence tests

We have performed two standard benchmark tests: the bending of a linear-elastic cantilever strip under the action of a tip load; and the stretching of a linear-elastic infinite plate with

a circular hole. In order to test the three-dimensional composite element, we solve these problems in three dimensions. The following norms and seminorms are used to quantify solution errors and gauge the performance of the element:

$$\|\boldsymbol{u}\|_0 = \left\{\int_\Omega |\boldsymbol{u}|^2 d\Omega\right\}^{1/2} \tag{5.28}$$

$$|\boldsymbol{u}|_E = \left\{\int_\Omega \sigma_{ij} u_{i,j} d\Omega\right\}^{1/2} \tag{5.29}$$

$$\|p\|_0 = \left\{\int_\Omega p^2 d\Omega\right\}^{1/2} \tag{5.30}$$

where $\boldsymbol{u}$, $\boldsymbol{\sigma}$ and p are the displacement, stress and pressure fields, respectively. Evidently, $\|\boldsymbol{u}\|_0$ and $\|p\|_0$ are the L_2 norms of $\boldsymbol{u}$ and p, respectively, whereas $|\boldsymbol{u}|_E$ is the energy semi-norm of $\boldsymbol{u}$. In calculations, all norms are computed by the five-point numerical quadrature rule described in the foregoing.

5.4.1.1 Cantilever Strip Problem

Next we consider the problem of a linear-elastic infinite cantilever strip under the action of a tip load P per unit length, Fig. 5.3. The strip has a uniform thickness t and length L. A system of orthonormal cartesian axes is chosen such that x_1 runs the width of the strip and x_3 points in its normal direction along thichness. Provided that the tip load is distributed appropriately over the end section of the strip, the solution to this problem is elementary (e. g., [48]), and is given by

$$u_1 = \frac{-Px_3}{6D}\{(6L - 3x_1)x_1 + (2+\overline{\nu})[x_3^2 - (t/2)^2]\} \tag{5.31}$$

$$u_2 = 0 \tag{5.32}$$

$$u_3 = \frac{P}{6D}[3\overline{\nu}x_3^2(L - x_1) + (4 + 5\overline{\nu})(t/2)^2 x_1 + (3L - x_1)x_1^2] \tag{5.33}$$

and

$$\sigma_{11} = -\frac{12Px_3}{t^3}(L - x_1) \tag{5.34}$$

$$\sigma_{22} = -\frac{12\nu Px_3}{t^3}(L - x_1) \tag{5.35}$$

$$\sigma_{13} = -\frac{6P}{t^3}[2(t/2)^2 - x_3^2] \tag{5.36}$$

$$\sigma_{33} = \sigma_{12} = \sigma_{23} = 0 \tag{5.37}$$

Here

$$D = \frac{Et^3}{12(1-\nu^2)} \tag{5.38}$$

$$\overline{\nu} = \nu/(1-\nu) \tag{5.39}$$

E and ν are the Young's modulus and Poisson's ratio of the material, respectively, and D is the bending stiffness of the plate.

Owing to the anti-symmetry of the problem about the neutral fiber of the plate, only the upper half of the plate is discretized. The analysis is carried out in three dimensions by discretizing a finite width W of the strip and subjecting the lateral surfaces $x_2 = 0$ and $x_2 = W$ to the boundary condition $u_2 = 0$. The section $x_1 = 0$ of the strip is built in. Nodal forces computed from (5.36) are computed over the end section $x_1 = L$. The numerical values of the parameters used in calculations are: $L = 24$, $W = 2$, $t = 4$, $P = 200$, $E = 3 \times 10^7$, and $\nu = 0.25, 0.4999$. The latter value of the Poisson's ratio renders the material nearly incompressible. The domain of analysis is partitioned into cubic blocks, and these blocks subsequently are discretized into tetrahedral elements as shown in Fig. 5.3.

Fig. 5.4 shows the dependence of various normalized error norms on mesh size(h). The error norms are normalized by the corresponding norm of the exact field. The convergence rates deduced from these plots are collected in Table 5.3. The convergence rate is the slope of the error *vs.* mesh-size curve in logarithmic axes. The theoretical rates of convergence of the errors $\| \boldsymbol{u}_h - \boldsymbol{u} \|_0$, $|\boldsymbol{u}_h - \boldsymbol{u}|_E$ and $\| p_h - p \|_0$ for simplicial tetrahedra are $k+1$, k and k, respectively, where k is the order of interpolation. As may be seen from Table 5.3, the computed rates in the L_2 norm of the displacement field is slightly below the theoretical value of linear interpolation, $k = 1$. By contrast, the convergence rates in pressure and in the energy norm are slightly better than those for linear interpolation. It is evident

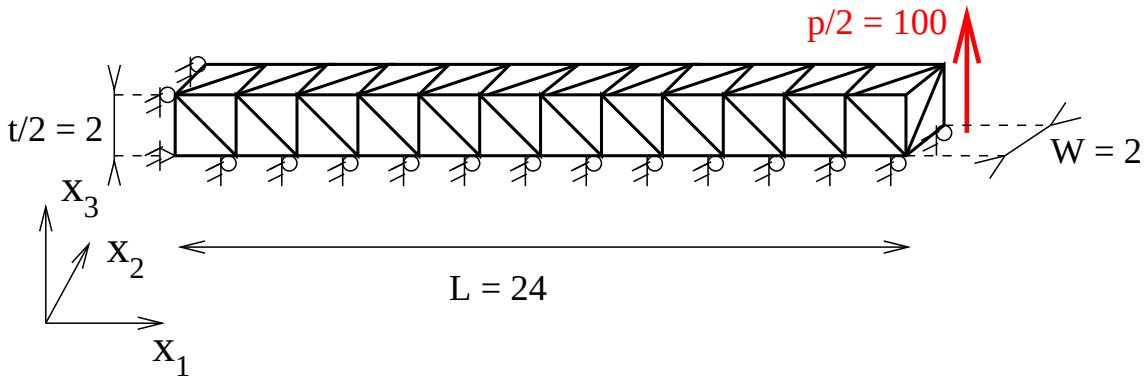

Figure 5.3: Sample mesh for the cantilever strip test problem showing the mesh design used in calculations.

ν	$\| \boldsymbol{u}_h - \boldsymbol{u} \|_0$	$\lvert \boldsymbol{u}_h - \boldsymbol{u} \rvert_E$	$\| p_h - p \|_0$
0.2500	1.8375	1.0669	1.0706
0.4999	1.8203	1.0500	1.1289

Table 5.3: Convergence rates for the cantilever strip test problem.

from the convergence plots that the accuracy of the element degrades somewhat in the near-incompressible limit. However, it is interesting to note that the convergence rates are maintained in that limit.

5.4.1.2 Infinite Plate with a circular hole problem

We consider an infinite plate containing a circular hole of radius a deforming in plane strain under the action of a remotely applied uniaxial tension σ, Fig. 5.5. We refer the plate of analysis to a system of polar coordinates (r, θ) and we denote by z the perpendicular coordinate. The analytical solution to this problem is (e. g., [48])

$$u_r = \frac{p(1+\nu)}{2E}\left[\frac{1-\overline{\nu}}{1+\overline{\nu}}r + \frac{a^2}{r} + \left(r - \frac{a^4}{r^3} + \frac{4a^2}{(1+\overline{\nu})r}\right)\cos 2\theta\right] \tag{5.40}$$

$$u_\theta = -\frac{p(1+\nu)}{2E}\left(r + \frac{a^4}{r^3} + \frac{1-\overline{\nu}}{1+\overline{\nu}}\frac{2a^2}{r}\right)\sin 2\theta \tag{5.41}$$

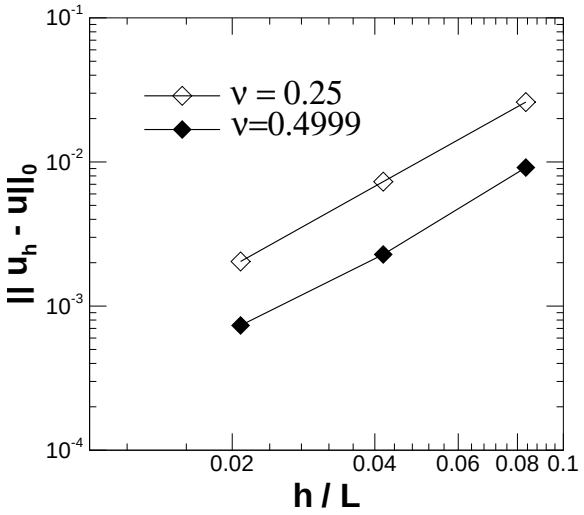

(a)

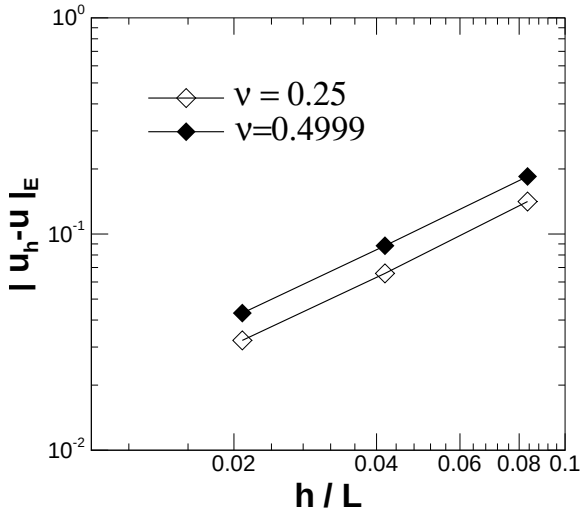

(b)

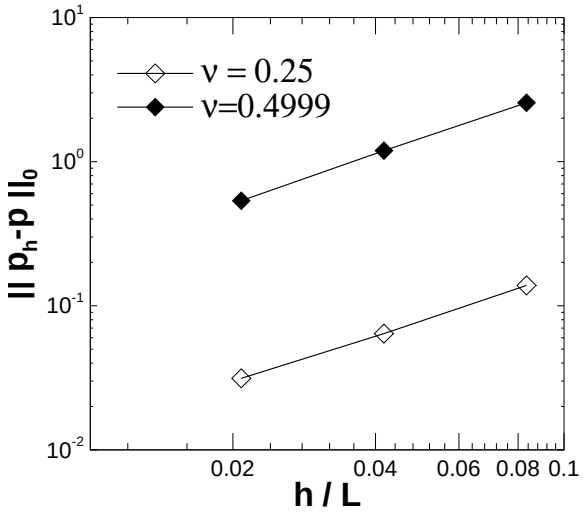

(c)

Figure 5.4: Convergence plots for the cantilever strip test problem: a) L_2-norm of displacement error; b) Energy norm of displacement error; c) L_2-norm of pressure error.

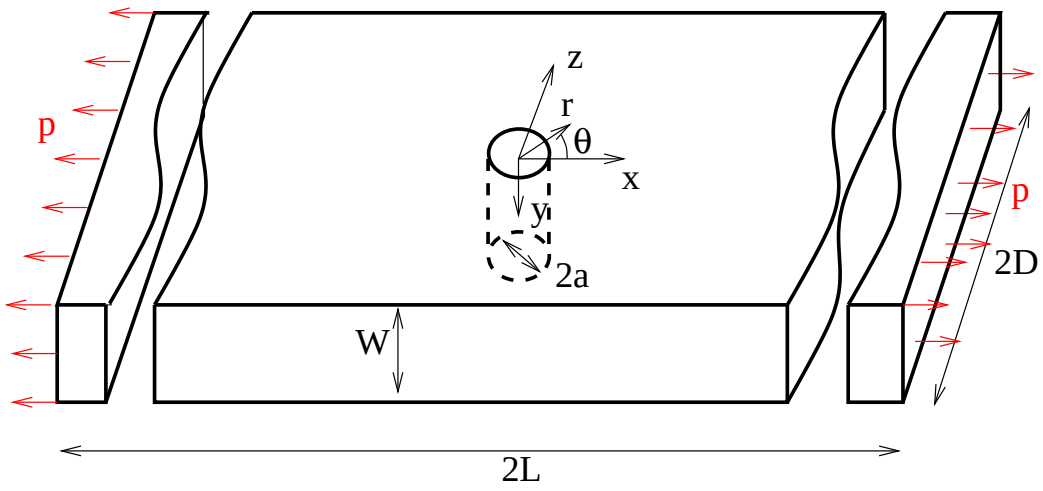

Figure 5.5: Infinite plate with a circular hole

and

$$\sigma_{rr} = \frac{p}{2}\left[\left(1-\frac{a^2}{r^2}\right)+\left(1+\frac{3a^4}{r^4}-\frac{4a^2}{r^2}\right)\cos 2\theta\right] \tag{5.42}$$

$$\sigma_{\theta\theta} = \frac{p}{2}\left[\left(1+\frac{a^2}{r^2}\right)-\left(1+\frac{3a^4}{r^4}\right)\cos 2\theta\right] \tag{5.43}$$

$$\sigma_{zz} = \nu p\left(1-\frac{2a^2}{r^2}\cos 2\theta\right) \tag{5.44}$$

$$\sigma_{r\theta} = -\frac{p}{2}\left(1-\frac{3a^4}{r^4}+\frac{2a^2}{r^2}\right)\sin 2\theta \tag{5.45}$$

$$\sigma_{rz} = \sigma_{\theta z} = 0 \tag{5.46}$$

Owing to the symmetries of the problem, the domain of analysis may be restricted to one quadrant of the (r,θ) plane. We carry out the calculations in three dimensions by discretizing a slab of material of thickness W. We additionally restrict the analysis to a finite square region in the (r,θ) plane of size $10a$. The exact analytical displacements (5.40-5.41) are prescribed on the remote edges of the domain of analysis. The numerical values of the parameters used in calculations are: $a = 0.1$, $W = 0.1$, $\sigma = 200$, $E = 3 \times 10^7$, and $\nu = 0.25, 0.4999$. As in the cantilever strip problem, this latter value of the Poisson's ratio tests the performance of the element in the near-incompressible range. A typical mesh used in calculations is shown in Fig. 5.6.

Fig. 5.7 shows the dependence of various normalized error norms on mesh size(h). The error norms are normalized by the corresponding norm of the exact field. The convergence

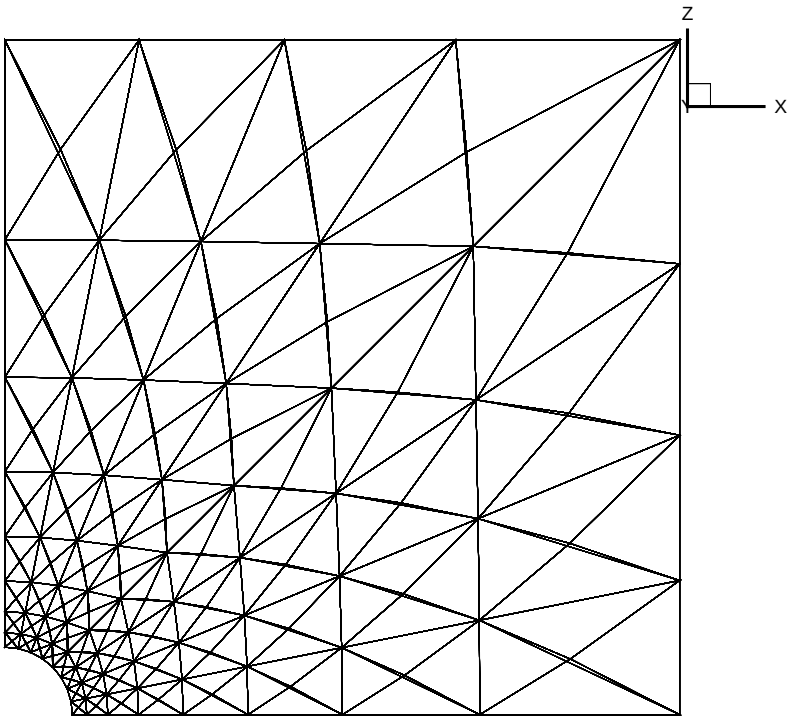

Figure 5.6: Sample mesh used in the plate with circular hole test problem

ν	$\| \boldsymbol{u}_h - \boldsymbol{u} \|_0$	$\lvert \boldsymbol{u}_h - \boldsymbol{u} \rvert_E$	$\| p_h - p \|_0$
0.2500	2.0511	1.0255	1.1145
0.4999	2.0148	1.0316	0.8848

Table 5.4: Convergence rates for the plate with a circular hole test problem.

rates deduced from these plots are collected in Table 5.4. As may be seen from this table, all convergence rates are slightly better than those corresponding to linear simplicial elements, except for the pressure error in the near-incompressible case, which lags somewhat behind the theoretical convergence rate. In general, the computed errors are larger in the near-incompressible case, which suggests a certain loss of accuracy of the element in that limit. However, despite this absolute accuracy loss, the rates of convergence appear to be maintained as the incompressible limit is approached.

5.4.2 Inf-Sup Test

Our final test is aimed at establishing whether the Babuška-Brezzi [37, 39] stability condition is satisfied by the composite CT3D element in the incompressible limit. The satisfaction

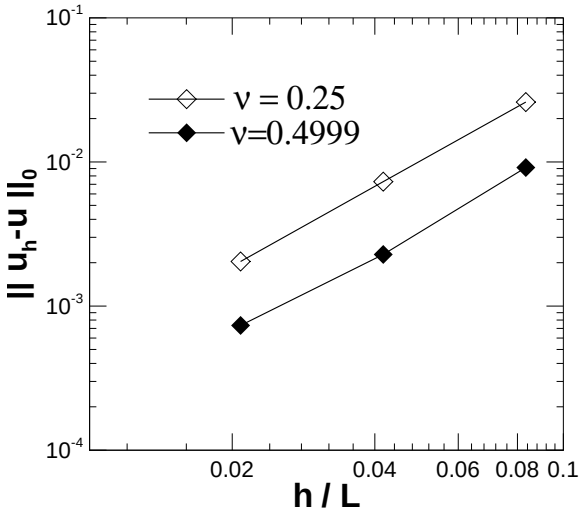

(a)

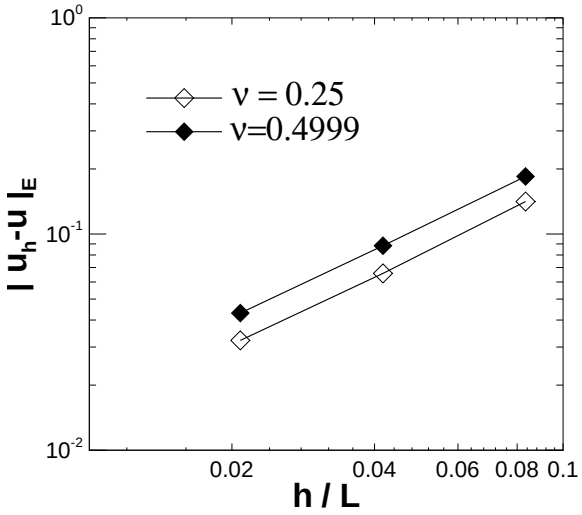

(b)

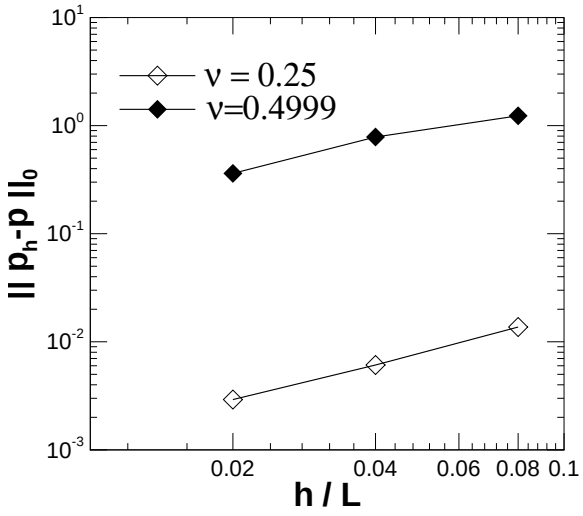

(c)

Figure 5.7: Convergence plots for the plate with a circular hole test problem: a) L_2-norm of displacement error; b) Energy norm of displacement error; c) L_2-norm of pressure error.

of the Babuška-Brezzi condition guarantees the convergence of finite-element schemes in the near-incompressible regime and, thus, establishes the absence of volumetric locking. Unfortunately, a rigorous verification of the Babuška-Brezzi condition for specific classes of elements and arbitrary meshes is difficult. Here, instead, we follow a procedure proposed by Chapelle and Bathe [42] (see also [38]) which is based on evaluating specific meshes and, therefore, furnishes a test–if not a definitive proof–of stability.

In Chapelle and Bathe inf-sup test, an upper bound β_h to the stability parameter is obtained as the square root of the minimum non-zero eigenvalue of the generalized symmetric eigenvalue problem:

$$\boldsymbol{G}_h \boldsymbol{v}_h = \lambda_h \boldsymbol{S}_h \boldsymbol{v}_h, \tag{5.47}$$

where $\boldsymbol{S}_h$ is the positive-definite symmetric matrix which delivers the L_2 norm $\| \boldsymbol{u}_h \|_0$, and $\boldsymbol{G}_h$ is the the positive semi-definite symmetric matrix which delivers the seminorm $\int_\Omega p_h \nabla \cdot \boldsymbol{u}_h d\Omega$. The procedure consists of computing the stability parameter β_h and verifying that it remains bounded below as the element size $h \to 0$.

We specifically consider a linear-elastic cubic block of Poisson's ratio $\nu = 0.4999$. In order to mesh the domain of analysis, we partition it into cubes and we subsequently discretize each cube into 12 composite elements. A sequence of meshes is generated by regular refinement and the stability parameter β_h is computed for each element size h. The result of the calculations is shown in Fig. 5.8. This figure suggests that β_h indeed remains bounded below as $h \to 0$ for the specific sequence of meshes under consideration. This asymptotic behavior of β_h suggests that the composite CT3D element is indeed free of volumetric locking.

5.5 Summary and conclusions

We have developed and analyzed a composite 'CT3D' tetrahedral element consisting of twelve 4-node linear tetrahedral elements and a linear assumed deformation defined over the entire domain of the composite element. The element is designed to have well-defined lumped masses and contact tractions in dynamic contact problems, which is accomplished by endowing the element with piecewise-linear displacement interpolation, while at the same time minimizing the number of volume constraints per element, which is accomplished by equipping the element with linear assumed deformations. The relation between displace-

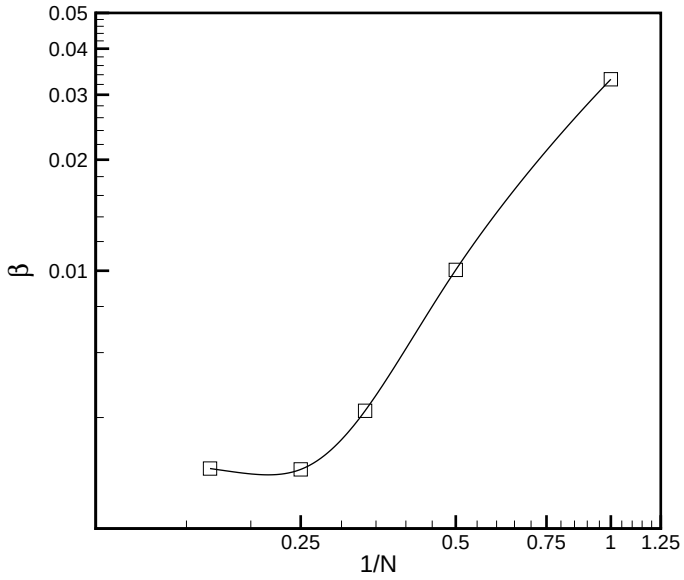

.

Figure 5.8: Asymptotic plot of the inf-sup value for the composite element.

ments and deformations is enforced weakly by recourse to the Hu-Washizu principle. The element arrays are formulated in accordance to the 'assumed- strain' prescription. However, our formulation of the element accounts for fully nonlinear kinematics. Integrals over the domain of the element are computed by a five-point quadrature rule.

We have verified that the element passes the patch test in arbitrarily distorted configurations. In addition, for compressible and near-incompressible materials the CT element has been found to possess convergence rate comparable to those of linear simplicial elements. We have also verified that the element satisfies the Babuška-Brezzi condition in the sense of Chapelle and Bathe [42, 38]. These tests suggest that the CT3D element can indeed be used reliably in calculations involving near-incompressible behavior such arises, e. g., in the presence of unconfined plastic flow.

Chapter 6

Conclusions and future work

In this thesis we proposed a novel method (VALE), which is finite element method generalized to account for horizontal variations. Consideration of horizontal variations enabled solution of undeformed (nodal) coordinates in addition to deformed coordinates. The solution so obtained satisfies configurational nodal force equilibrium in addition to nodal force equilibrium. The resulting mesh adaption scheme provides the optimal mesh and provides mesh optimality criterion. Further, this method can be used for the solution of reference configuration in inhomogeneous case. Also, the resulting variational integrator has good long-term energy behavior and provides for the update algorithm for the undeformed coordinates.

6.1 Future Work

Here are the some of the interesting topics of research which are related to the work in this thesis.

VALE: It will be very interesting to investigate the uniqueness of the minima, i.e., convexity, in the combined space of deformed and undeformed coordinates. This has consequences for uniqueness of optimal mesh and solution procedure for static case. This will also help the development of effective preconditioners for the efficient numerical solution. Further, development of explicit time integrator within VALE framework could go a long way for the simulation of contact-impact phenomena as it would significantly improve stable time-step (corresponding to CFL condition) and hence efficient numerical simulation. Also combining explicit VALE integrator with AVI [28] will provide very efficient variational integrators for

explicit computations.

Shape Optimization: As mentioned earlier, VALE can be used for the case when finite deformation effects are important which is not amenable to analytical treatment as in the case of interface-free surface interaction. Also, VALE in conjunction with gradient flow theory [33] can be used for the study of diffusion induced morphological transformations. This has important applications in the life estimation of turbine blades made of precipitation hardened super alloys, the study of Ostwald ripening, etc.

Structural Optimization: In structural optimization methods based on material distribution are very popular [35, 36] for the design of optimal topology. However these methods have the disadvantage of checker-board formation and scale insensitivity. However when VALE is used for design of optimal topologies these spurious effects should not be present as these are energetically unfavorable. In this regard it would be interesting to study the application of VALE method for the design of optimal topologies.

Ballistic Penetration of Solids: In the numerical modeling of ballistic penetration of solids, elements in the vicinity of contact regions undergo large deformation. This in turn reduces stable time step for the explicit time integration, which is undesirable for the efficient numerical modeling. However, mesh adaption with VALE not only resolves steep gradients close to contact zone, but also increases stable time step.

Bio-fluid Mechanics : In the cardiovascular system, blood vessels are flexible, because of which fluid-structure interaction becomes very important. This can be accounted for in an exact manner my modeling both blood and blood vessels within the Lagrangian frame work [34]. Further, at the entry and exit of the vessels boundary conditions are Eulerian. This Euler-Lagrange coupling can be modeled in a variationally consistent manner in VALE framework. In addition, elements at the interface of blood and blood vessels have tendency to get distorted in the absence of mesh adaption due to boundary layer formation. However mesh adaption ensures good quality mesh.

Fracture Mechanics: As demonstrated earlier, J-integral can be evaluated accurately

and efficiently in this framework. Further, in the dynamic fracture simulation, when done in conjunction with cohesive elements, optimal mesh obtained should be oriented in such a manner as to provide cohesive surface along crack growth direction and hence improves accuracy of the numerical solution.

Bibliography

[1] Gurtin, M.E. *Configurational Forces as Basic Concepts of Continuum Physics,* Springer-Verlag Inc., New York, 2000.

[2] Gurtin, M.E. The nature of configurational forces. *Arch. Rational Mech. Anal. 1995; 131:67–100.*

[3] Hughes, T.J.R. *The Finite Element Method,* Dover Publications Inc., New York, 2000.

[4] Budiansky, B. and Rice, J.R. Conservation laws and energy release rates. *Journal of Applied Mechancis 1973; 40:201–203.*

[5] Rice, J.R. A path independent integral and the approximate analysis of strain concentration by notches and cracks.' *Journal of Applied Mechancis 1968; 35:379–386.*

[6] Rice, J.R. Mathematical analysis in the mechanics of fracture. *Fracture, an advanced treatise, vol. II, ed., Liebowitz, H., Academic Press, 1968; 35:191–311.*

[7] Shih, C.F., Moran, B. and Nakamura, T. Energy release rate along a three dimensional crack front in a thermally stresses body. *International Journal of Fracture 1986; 30:79–102.*

[8] Moran, B. and Shih, C.F. A general treatment of crack tip contour integrals. *International Journal of Fracture 1987; 35:295–310.*

[9] Eshelby, J.D. The elastic energy-momentum tensor. *Journal of Elasticity 1975; 5:321–335.*

[10] Eshelby, J.D. The energy-momentum tensor in continuum mechanics. *Inelastic behavior of solids, ed., Kanninen, M.F., et. al., McGraw-Hill, New York 1970.*

[11] Eshelby, J.D. The continuum theory of lattice defects. *Solid state physics, vol III, eds., Seitz, F., and Turnbull,D., Academic Press, 1956.*

[12] Shewchuk, J.R. An introduction to the conjugate gradient method without agonizing pain. *http://www.cs.berkeley.edu/ jrs.*

[13] Kane, C., Marsden, J.E., Ortiz, M. and West, M. Variational integrators and the newmark algorithm for conservative and dissipative mechanical systems. *International Journal of Numerical methods in engineering 2000; 49:1295–1325.*

[14] Maugin, G.A. *Material Inhomogeneities in Elasticity,* Chapman and Hall., London, 1993.

[15] Johnson, W.C. and Cahn, J.W. Elastically induced shape bifurcations of inclusions. *Acta Metall., 1984; 32:1925–1933.*

[16] Thomson, M.E., Su, C.S. and Voorhees, P.W. The equilibrium shape of a misfitting precipitate. *Acta Metall. Mater., 1994; 42:2107–2122.*

[17] Schmidt, I. and Gross, D. The equilibrium shape of an elastically inhomogeneous inclusion. *J. Mech. Phys. Solids, 1997; 45:1521–1549.*

[18] Jog, C.S., Sankarasubrmanian, R. and Abinandan, T.A. Symmetry-breaking transitions in equilibrium shapes of coherent particles. *J. Mech. Phys. Solids, 1997; 48:2363–2389.*

[19] Rob Philips. *Crystals, Defects and Microstructures,* Cambridge University Press., Cambridge, 2001.

[20] Radovitzky, R. and Ortiz, M. Error estimation and adaptive meshing in strongly nonlinear dynamic problems. *Comput Meth Appl mech, 1999; 172:203–240.*

[21] Molinari, J.F. and Ortiz, M. Three dimensional adaptive meshing by subdivision and edge-collapse in finite-deformation dynamic-plasticity problems with application to adiabatic shear banding. *Int. J. Num. Meths. Engg., 2002; 53:1101–1126.*

[22] Zienkiewicz, O.C. and Zhu, J.Z. A simple error estimator and adaptive procedure for practical engineering analysis. *Int. J. Num. Meths. Engg., 1987; 24:337–357.*

[23] Mueller, R. and Gross, D. 3D simulation of equilibrium morphologies of precipitates. *Computational Materials Science,1998; 11:35–44.*

[24] Leo, P.H., Lowengrub, J.S. and Jou, J.H. A diffusive interface model for microstructural evolution in elastically stressed solids. *Acta mater., 1998;.46:2113–2130.*

[25] Anderson, T.L. *Fracture Mechanics,* CRC press, Boca Raton, 1995.

[26] Shephard, M.S., Gallagher, R.H. and Abel, J.F. The synthesis of near-optimum finite element meshes with interactive computer graphics. *Int. J. Num. Meths. Engg., 1980; 15:1101–1126.*

[27] Fetecau, R.C., Marsden, J.E. and West, M. Variational multisymplectic formulations of non-smooth continuum mechanics. *Int. J. Num. Meths. Engg., 2002; 15:1101–1126.*

[28] Lew, A.J., Marsden, J.E., Ortiz, M. and West, M. Asynchronous Variational Integrators. *Archive for rational mechanics and analysis, in press.*

[29] Kane, C., Marsden, J.E. and Ortiz, M. Symplectic-energy-momentum preserving variational integrators. *Journal of mathematical physics, 1999;.40:3353–3371.*

[30] Carlson, N.N. and Miller, K. Design and application of a gradient-weighted moving finite element code I: In one dimension. *SIAM Journal of Scientific Computing , 1998;.19:728–765.*

[31] Carlson, N.N. and Miller, K. Design and application of a gradient-weighted moving finite element code II: in two dimensions. *SIAM Journal of Scientific Computing , 1998; 19:766–798.*

[32] Miller, K. and Miller, R. Moving Finite Elements, Part I. *SIAM Journal of Numerical Analysis, 1981; 18:1019–1032.*

[33] Carter, W.C., Taylor, J.E. and Cahn, J.W. Variational methods for microstructural-evolution theories. *JOM,1997; 12:30–36.*

[34] Thoutireddy, P. and Ortiz, M. Variational-velocity Lagrangian formulation of fluid flow. *Unpublished research.*

[35] Bendsoe, M.P. and Kikuchi, N. Generating optimal topologies in structural design using homogenization method. *Computer methods in applied mechanics in engineering, 1988; 71:197–224.*

[36] Jog, C.S., Haber, R.B. and Bendsoe, M.P. Topology design with optimized self-adaptive materials. *Int. J. Num. Meths. Engg., 1994; 37:1323–1350.*

[37] Babuška, I. Error bounds for finite element method *Numerische Mathematik, 1971; 16:322–333.*

[38] Bathe, K.J. *Finite Element Procedures,* Prentice-Hall of India Pvt. Ltd., New Delhi,1997.

[39] Brezzi, F. On the existence, uniqueness and approximation of saddle-point problems arising from Lagrange Multipliers. *RAIRO, 1974; 8:129–151.*

[40] Camacho, G.T. *Computational modeling of impact damage and penetration of brittle and ductile materials.* Ph.D Dissertation, Brown University, Providence,RI,1995.

[41] Camacho, G.T and Ortiz, M. Computational modeling of impact damage in brittle materials. *Int. J. Solids and Struct. 1996;33:2899–2938.*

[42] Chappelle, D. and Bathe, K.J. The inf-sup test. *Computers and Structures 1993;47:537–545.*

[43] Guo, Y., Ortiz, M., Belytschko, T. and Repetto, E.A. Triangular composite finite elements. *Int. J. Numer. Meths. Engg., 2000; 47:287–316.*

[44] Hughes, T.J.R. Generalization of selective integration procedures to anisotropic and nonlinear media. *Int. J. Numer. Meths. Engg., 1980; 15:1413–1418.*

[45] Simo, J.C. and Hughes, T.J.R. On the variational foundation of the assumed strain methods. *J. Appl. Mech., 1986; 53:51–54.*

[46] Zienkiewicz, O.C., Liu, Y.C. and Huang G.C. Error estimates and convergence rates for various compressible materials. *Int. J. Numer. Meths. Engg., 1989; 28:2191–2202.*

[47] Rivara, M.C. New longest-edge algorithms for the refinement and/or improvement of unstructured triangulations. *Int. J. Numer. Meths. Engg., 1997; 40:3313–3324.*

[48] Timoshenko, S.P. and Goodier, J.N. *Theory of Elasticity, 3rd Ed.* McGraw-Hill, New York,1970.

[49] Knap, J. *Private communication.*

[50] Maute, K. and Ramm, E. Adaptive Topology optimization. *Structural Optimization, 1995; 10:100–112.*